Solid Earth, 17, 991–1010, 2026
https://doi.org/10.5194/se-17-991-2026

Solid Earth Open Access EGU

Structural controls on lithium-bearing fluid flow in Clayton Valley, Nevada

Adam J. Cawood[1,2], **David A. Ferrill**[1], **Isaac A. Rangel-Landeros**[3], **Kristina L. Butler**[3,4], **Daniel E. Ibarra**[5,6], **Zachary T. Sickmann**[3], **Madigan R. Blake**[3], **Brandon Swanson**[7], **Kevin J. Smart**[1], **Lee Ann Munk**[8,9], **David F. Boutt**[10], **Lisa D. Stockli**[11], **Daniel F. Stockli**[11], **and Catherine A. Gagnon**[5,6]

[1]Southwest Research Institute, 6220 Culebra Rd., San Antonio, Texas, 78238, USA
[2]Department of Earth and Environmental Sciences, Syracuse University, Syracuse, New York, USA
[3]Department of Sustainable Earth Systems Sciences, The University of Texas at Dallas, Richardson, Texas 75080, USA
[4]Department of Geoscience, University of Wisconsin–Madison,1215 West Dayton Street, Madison, Wisconsin 53706, USA
[5]Department of Earth, Environmental and Planetary Sciences, Brown University, Providence, Rhode Island 02912, USA
[6]Institute at Brown for Environment and Society, Brown University, Providence, Rhode Island 02912, USA
[7]Albemarle Corporation, NV-265, Silver Peak, Nevada, 89047, USA
[8]Department of Geosciences, University of Alaska Fairbanks, 308 Reichardt Bldg., 1930 Yukon Dr., Fairbanks, AK 99775, USA
[9]Geophysical Institute, University of Alaska Fairbanks, 2156 Koyukuk Dr., Fairbanks, AK, 99775, USA
[10]Department of Earth, Geographic, and Climate Sciences, University of Massachusetts Amherst, Amherst, Massachusetts 01003, USA
[11]Jackson School of Geosciences, University of Texas, Austin, TX, 78712-1722, USA

Correspondence: Adam J. Cawood (ajcawood@syr.edu)

Received: 20 March 2026 – Discussion started: 1 April 2026
Revised: 17 July 2026 – Accepted: 31 July 2026 – Published: 19 August 2026

Abstract. Lithium brine systems are critical resources for the energy transition, yet the mechanisms governing lithium mobilization, transport, and concentration remain poorly constrained. In particular, the role of fault and fracture networks in controlling fluid flow and associated lithium distribution is not well resolved. New analyses of calcite-mineralized faults and opening-mode fractures, and paleo-spring deposits from Clayton Valley, Nevada are interpreted to record lithium-bearing fluid flow through > 10 Myr of Basin and Range extension. Calcite U–Pb ages related to Basin and Range extension range from 15.4 ± 6.4 to 4.2 ± 2.3 Ma. Clumped-isotope formation temperatures of vein calcites span 24.6 ± 4.1 to 139.2 ± 12.6 °C, and bulk lithium concentrations of veins and paleo-spring deposits span < 2 to 460 ppm. These results indicate that fault and fracture networks repeatedly served as conduits for lithium-bearing fluids through basement, along basin margins, and within basin-fill strata throughout basin evolution. Lithium concentrations vary systematically with host setting, with the highest values recorded in basin-fill-hosted veins and spring deposits and generally lower values in basement-hosted and basin-bounding fault veins. Several veins containing measurable lithium yield U–Pb ages older than the ~ 6 Ma Rhyolite Ridge tuff, the dominant volcanic lithium source unit in the region, suggesting that structurally focused lithium-bearing fluid circulation locally predated its emplacement. The highest lithium concentrations, however, are generally associated with younger veins that postdate the tuff. Temperature and stable isotope constraints indicate dominantly meteoric fluids advected to depth and focused along faults, suggesting that lithium transport and enrichment in Clayton Valley does not necessarily require ascent of lithium-enriched magmatic fluids along deeply rooted crustal-scale faults. Although fault-controlled lithium enrichment has been recognized previously, this study provides direct evidence for long-lived structurally focused fluid flow associated with lithium transport over multi-Myr timescales.

Published by Copernicus Publications on behalf of the European Geosciences Union.

1 Introduction

Closed-basin brines host some of the world's largest continental lithium accumulations and play a central role in the global lithium supply (Bradley et al., 2017; Coffey et al., 2021). Formation of these systems requires the coincidence of suitable lithium sources, hydrologic or tectonic basin closure, arid climate, and basin-scale processes capable of mobilizing, transporting, and concentrating lithium over geologic timescales (Bradley et al., 2013; Munk et al., 2016, 2025). In basin-hosted lithium systems, lithium enrichment is commonly attributed to meteoric leaching of silicic volcanic rocks and ash, volcaniclastic basin fill, and, in some cases, deeper basement lithologies, followed by progressive concentration within evolving basin depocenters (Price et al., 2000; Coffey et al., 2021; Munk et al., 2016, 2025; Darin et al., 2025; Thompson et al., 2025).

At the deposit-model scale, "active faulting appears to be involved in all lithium basins" (Bradley et al., 2013), reflecting the role of tectonically driven subsidence and/or uplift in creating accommodation space and aquifer systems capable of hosting economic volumes of lithium-rich brines. Across tectonic settings, structural and tectonostratigraphic development (including basin formation) is accompanied by brittle deformation, during which fault and fracture networks form, link, and are reactivated through time (e.g., Hancock, 1985; Cawood et al., 2021; Ferrill et al., 2021). As a result, tectonically developed basins – including active lithium basins in both extensional and contractional regimes – are characterized by pervasive fault and fracture networks that exert a strong influence on subsurface structure and permeability (e.g., Bradley et al., 2013; Marazuela et al., 2020; Putzolu et al., 2025). Fault and fracture networks are therefore fundamental components of groundwater flow in these settings, exerting first-order controls on permeability, locally focusing or impeding fluid migration (e.g., Caine et al., 1996; Bense et al., 2013), enabling fluid flow within basins, and potentially providing pathways for interbasin-scale solute transport over tens of kilometers (e.g., Heilweil and Brooks, 2011; Munk et al., 2016).

Faults and fractures have been invoked as constructive pathways that promote lithium enrichment by focusing fluid flow, enhancing water–rock interaction, and linking deep and shallow reservoirs, particularly in volcano–sedimentary settings where hydrothermal alteration and lithium enrichment are spatially associated with structural zones (e.g., Bradley et al., 2013; Marazuela et al., 2020; Benson et al., 2023). Conversely, faults have also been proposed to facilitate fluid leakage, potentially compromising lithium retention by allowing solute-rich fluids to escape basin reservoirs (e.g., Watts, 2025). In most cases, these interpretations are based on spatial associations, and basin-scale hydrogeologic models, or brine geochemistry (Heilweil and Brooks, 2011; Coffey et al., 2021), rather than direct records of fluid flow along individual fault or fracture systems. Consequently, the timing, depth, and persistence of fault-controlled fluid circulation in active lithium basins remain insufficiently constrained.

A key limitation in evaluating the role of faults in lithium systems is the lack of direct constraints on fault-hosted fluid flow through time. Mineral veins precipitated within faults and fractures, and spring travertine deposits associated with faults at depth, provide direct geochemical records of fluids that circulated along discrete structures (Fyfe et al., 1978; Eaton, 1982; Chen et al., 2024). Such records have not (to our knowledge) been directly constrained by absolute geochronology of structural pathways in active lithium basins, however. Here, we analyze calcite veins hosted in faults and fractures, together with spring and travertine deposits interpreted to reflect structurally focused fluid flow, from the vicinity of the Silver Peak lithium mine in Clayton Valley, Nevada. Sampling spans a range of structural settings, structural positions, host lithologies, and geographic locations across the Clayton Valley region, providing a first-order basin-scale assessment of fault- and fracture-controlled fluid flow. We integrate U–Pb calcite geochronology, clumped-isotope thermometry, and lithium geochemistry to directly constrain the timing, depth, and geochemical character of fluids circulating along brittle structures during Basin and Range extension. Our approach evaluates the role of faults and fractures as pathways for lithium-bearing fluids within an active closed-basin lithium system, providing new constraints on the processes that link deformation, fluid flow, and lithium redistribution through time.

2 Geologic Setting

Clayton Valley is an extensional basin in the central Basin and Range province of western Nevada, located along the eastern margin of the Walker Lane belt (Fig. 1a). Clayton Valley is flanked by uplifted and faulted Proterozoic to Paleozoic basement rocks and overlain by Miocene and younger volcanic and volcaniclastic units associated with regional magmatism in the central Basin and Range province (Fig. 1b, c). Extension in Clayton Valley initiated at ca. 16 Ma via detachment faulting in the Silver Peak-Lone Mountain extensional complex and initiation of the Mineral Ridge detachment system (Stewart and Diamond, 1990; Oldow et al., 1994; Diamond and Ingersoll, 2002) which occupies an extensional structural stepover linking right-lateral strike slip faults of the Furnace Creek fault system with the central Nevada Walker Lane fault network (Oldow et al., 2008). Extension on this system was accompanied by upper-plate extension and exhumation of lower-plate rocks (Stewart and Diamond, 1990; Diamond and Ingersoll, 2002). By ∼ 6 Ma, detachment activity waned and deformation localized onto higher-angle normal faults, coincident with half-graben development, focused subsidence, and late-Miocene silicic volcanism that emplaced key lithium-source materials (Ogilvie, 2023; Ogilvie et al., 2023; Darin et al., 2025; Cawood et al., 2025; Rangel et al., 2025).

Early Miocene slip on the Mineral Ridge detachment likely produced a broad basin filled by lower Esmeralda Formation strata, sourced from eastern and western highlands (Stewart and Diamond, 1990; Diamond and Ingersoll, 2002). Ongoing extension, including relatively recent deformation from the Late Miocene onwards (~ 6 Ma and younger), generated mostly west-dipping, higher-angle normal faults that localized Pliocene–Pleistocene lacustrine and volcaniclastic sedimentation and controlled accommodation space for volcano-sedimentary units (Fig. 1d; Ogilvie et al., 2023; Darin et al., 2025; Cawood et al., 2025; Rangel et al., 2025). Basin fill comprises interbedded tuffs, ash layers, lacustrine deposits, conglomerates, and sandstones, producing a heterogeneous stratigraphy that thickens eastward into fault-bounded sub-basins (Stewart and Diamond, 1990; Diamond and Ingersoll, 2002).

Lithium enrichment in Clayton Valley reflects the combined influence of basin structure, volcanic input, and hydroclimate evolution (Coffey et al., 2021; Gagnon et al., 2023; Bhattacharya et al., 2024). Basin fill comprises lithium-enriched volcaniclastic strata, lacustrine mudstones, and evaporite deposits (20–2000 ppm Li; Coffey et al., 2021), and brines that collectively host one of the world's largest continental lithium accumulations (Kunasz, 1974; Davis and Vine, 1979; Davis et al., 1986; Price et al., 2000; Gagnon et al., 2023; Bhattacharya et al., 2024). Early studies linked lithium brines to silicic volcanic centers, identifying volcanic glass and ash as primary lithium sources (Price et al., 2000). Subsequent work indicated that volcanogenic inputs are supplemented by complex basin-scale hydrologic mixing involving shallow meteoric waters and deeper basin fluids (Munk et al., 2011). Basin-fill clays and tuffs contain elevated lithium concentrations (20–2000 ppm), with up to ~ 30 % of the lithium present in soluble form, and total basin inventories of 24–58 Mt of lithium stored in sediment and brine (Coffey et al., 2021). Basin architecture governs both routing and storage of lithium, and prior studies have conceptualized multiple end-member pathways for lithium transport within Clayton Valley, including interbasin inflow, intrabasin volcanogenic and sediment leaching and redistribution, and deeper basin-scale fluid circulation (e.g., Munk et al., 2016; Coffey et al., 2021).

3 Materials and Methods

3.1 Field work and sample collection

Thirty calcite-bearing samples were collected in and around Clayton Valley, Nevada (Figs. 1 and 2). These include 15 calcite vein samples hosted in basement rocks, two samples from basin-bounding faults, nine calcite vein samples hosted within basin-fill strata, and four travertine samples associated with fossil carbonate spring deposits. Sampling of fault- and fracture-hosted calcite veins deliberately targeted relatively late-stage brittle structures interpreted to be related to Basin and Range extension, while avoiding earlier vein sets and fracture arrays (e.g., en echelon tension gashes) preserved in the basement. Interpretation of Basin and Range-related structures was based on brittle deformation style, relatively planar geometries, and field relationships, particularly where faults and fractures appeared to crosscut earlier fabrics, vein sets, or deformation features. Despite these criteria, some sampled structures may represent reactivated older faults and fractures that were subsequently mineralized during later fluid-flow events. For these structures, strike and dip were measured at each site, with slip rake and displacement recorded where preserved (Tables S1 and S2 in the Supplement). Sampling locations were selected to capture a range of structural settings and positions in the Clayton Valley area rather than focusing on a single fault zone or set of structures. Travertine samples were collected from surface carbonate mounds developed on the basin floor and are not associated with active spring discharge, although some of these springs were active as recently as the mid 1900's prior to lithium brine production (Kunasz, 1974).

3.2 Analytical Methods

Compositional analysis was performed by ALS Geochemistry Testing and Analysis in Reno, Nevada using the *ME-MS89L Super Trace* inductively coupled plasma mass spectrometry (ICP-MS) method. Detection ranges for this method are reported at ~ 2–25 000 parts per million (ppm) for lithium and other trace elements (ALS, 2025). All 30 of the calcite samples described in Sect. 3.1 were analyzed for trace element composition.

U–Pb calcite geochronology was conducted at the UTChron Laboratory, University of Texas at Austin, using in situ laser ablation ICP-MS methods. Analyses included petrographic characterization and screening for U content prior to dating. Calcite veins were analyzed as thick sections ($\sim 60\,\mu m$), with approximately 40 ablation spots per sample, following the protocols of Palacios-García et al. (2023). Measurements were performed using a high-resolution magnetic-sector ICP-MS coupled to a 193 nm excimer laser. Data reduction and age calculations were performed using Iolite4 (Paton et al., 2011) with the VisualAge UcomPbine data reduction scheme (Chew et al., 2014). A ^{207}Pb-based common-Pb correction was applied using the primary calcite reference material WC-1 (Roberts and Walker, 2016; Roberts et al., 2017). Elemental and isotopic fractionation were corrected through interspersed analyses of WC-1, secondary calcite reference material RA138, and NIST-614 glass (Hollocher and Ruiz, 1995; Jochum et al., 2005; Kaiyun et al., 2014). Secondary reference material RA138 yielded a mean $^{206}Pb / ^{238}U$ age of 308 ± 4 Ma (MSWD = 4.5; $n = 109$), consistent with published values (Guillong et al., 2024). U–Pb data were plotted on Tera–

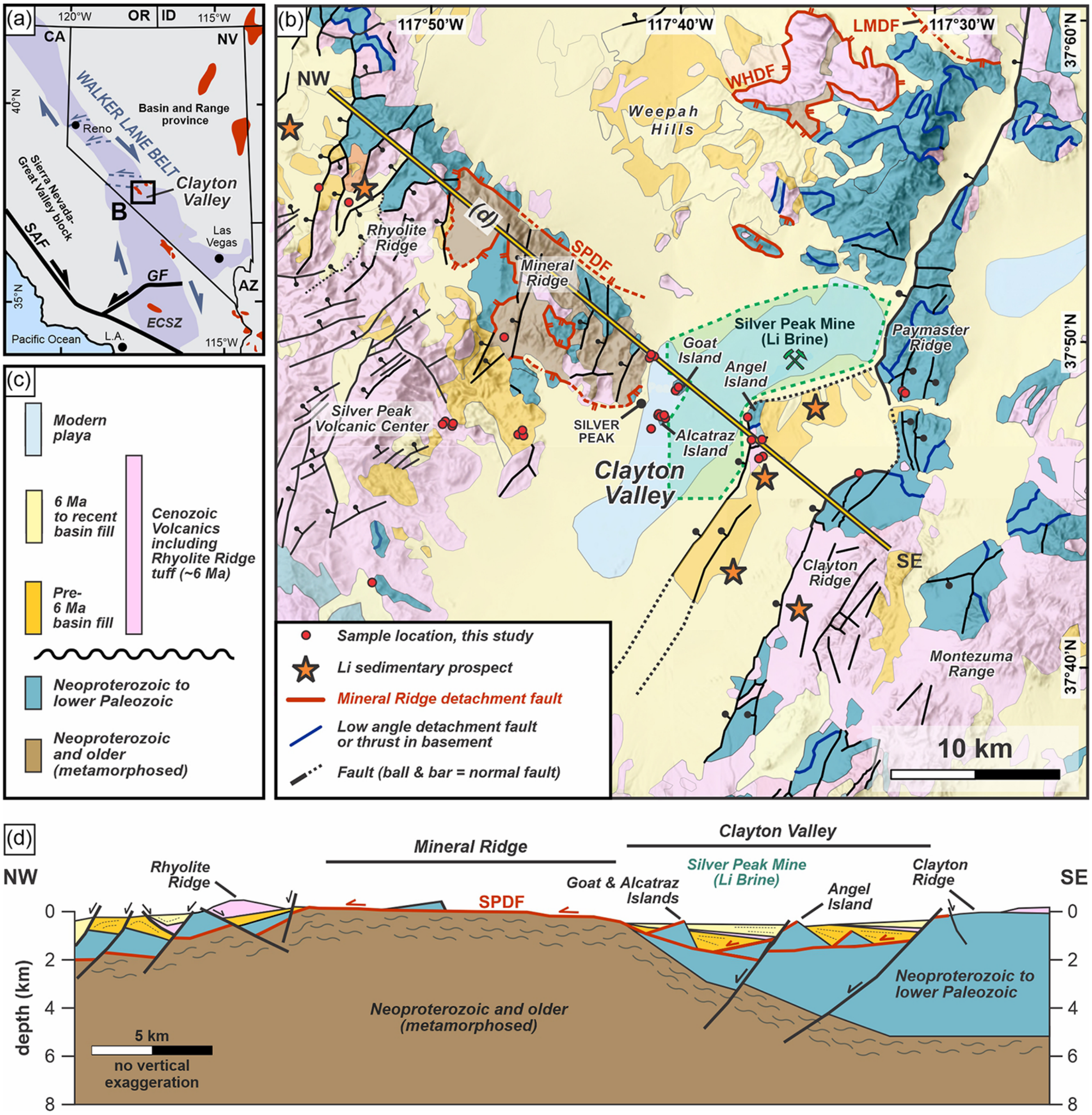

Figure 1. Geologic map of Clayton Valley, Nevada. **(a)** Regional tectonic provinces of the southwestern United States, adapted from Darin et al. (2025). Red polygons mark the position of exposed metamorphic core complexes in the region, including the Mineral Ridge detachment system in Clayton Valley; modified from Davis et al. (2023). **(b)** Geologic map of the greater Clayton Valley region, modified from Albers and Stewart (1972), U.S. Geological Survey (2024), and Darin et al. (2025). **(c)** Generalized stratigraphy. Formation names and approximate ages after Diamond and Ingersoll (2002). **(d)** Schematic NW–SE cross section across the study area (location shown in panel **b**), illustrating the first-order tectonostratigraphic framework of Clayton Valley. Cross-section geometry is based on Diamond and Ingersoll (2002), Ogilvie et al. (2023), Darin et al. (2025), and subsurface constraints from Coffey et al. (2021). Abbreviations: OR, Oregon; ID, Idaho; NV, Nevada; CA, California; AZ, Arizona; SAF, San Andreas Fault; GF, Garlock Fault; L.A., Los Angeles; ECSZ, Eastern California Shear Zone; SPDF, Silver Peak detachment fault; WHDF, Weepah Hills detachment fault; LMDF, Lone Mountain detachment fault.

Wasserburg diagrams (Tera and Wasserburg, 1972), and lower-intercept ages were calculated using IsoplotR (Vermeesch, 2018). In total, 26 samples were analyzed for U–Pb geochronology.

Carbonate clumped isotope thermometry was conducted at Brown University. Each sample (∼ 50 mg, depending on carbonate content) was reacted with 104 % orthophosphoric acid at 90 °C for 20 min and the resulting CO_2 was continuously frozen in liquid N_2 throughout the reaction. Cryogenic

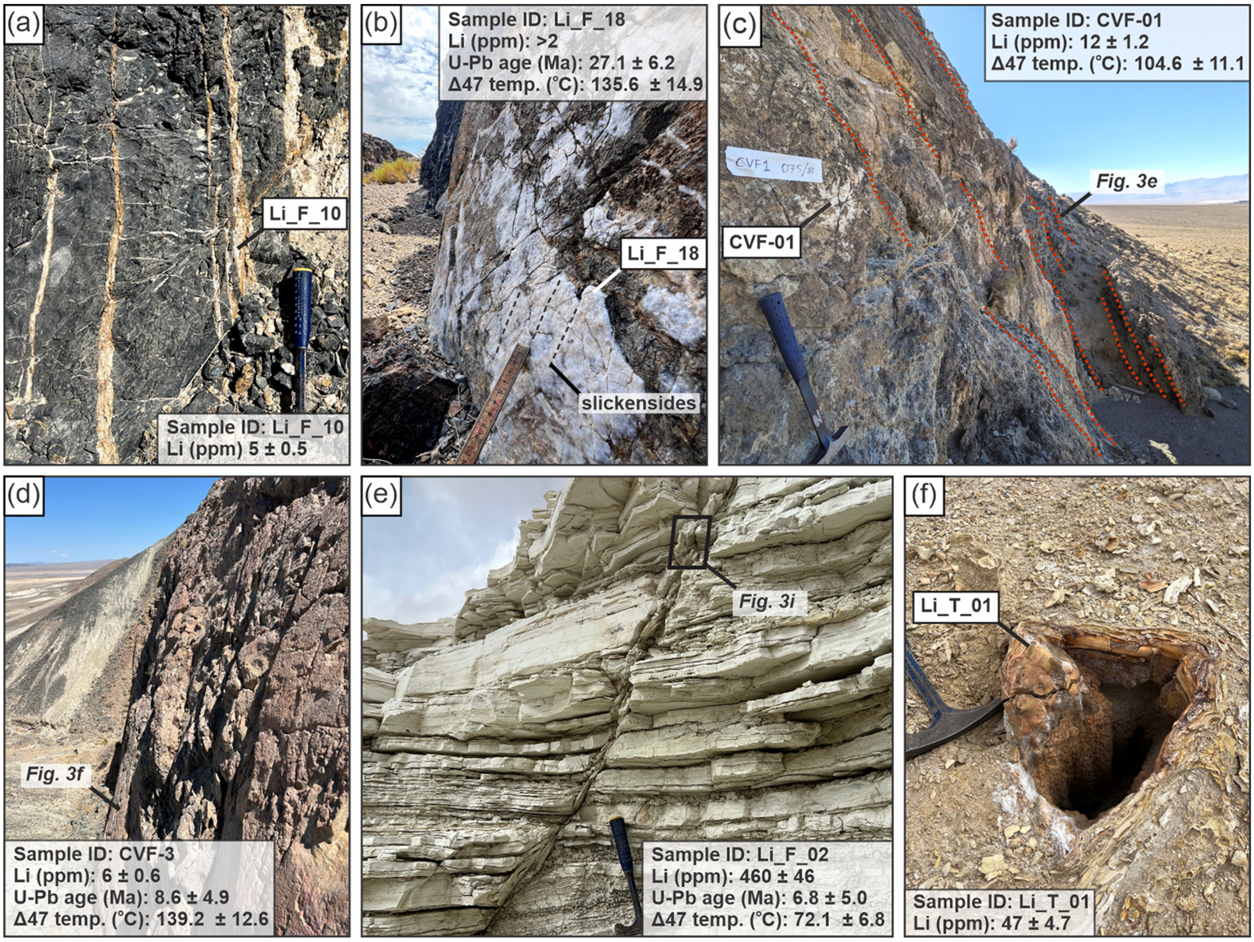

Figure 2. Examples of sample types and settings collected for geochemical analysis. **(a)** Basement-hosted opening-mode veins. **(b)** Basement-hosted normal fault. This structure is characterised by slickensided calcite mineralization. View to the east. **(c, d)** Basin-bounding faults. **(c)** A west-dipping normal fault zone that defines the eastern margin of Clayton Valley. The fault zone includes multiple slip surfaces (red dotted lines) in basement rocks and overlying alluvial fan deposits. View to the south. **(d)** Major fault on the west flank of Angel Island; view to the north; fault scarp is ca. 15 m high. **(e)** Calcite-mineralized dilational normal fault hosted within basin-fill sediments; view to the north. **(f)** Paleo–hot spring deposits associated with fault-controlled fluid discharge and spring precipitation.

and gas chromatographic separations were conducted using the Protium Isotopologue Batch Extraction (IBEX) system to purify the gas before introduction into a Thermo MAT 253 Plus dual-inlet isotope ratio mass spectrometer. Carbonate isotopic clumping was quantified to estimate calcite crystallization temperatures using the Δ_{47} parameter [$\Delta_{47} = (R_{47}/R^*_{47} - 1) \times 1000$], where R_{47} represents the measured abundance of mass 47 isotopologues relative to mass 44 in CO_2, and R^*_{47} is the expected stochastic distribution (Ghosh et al., 2006). Measured δ_{45}, δ_{46}, and δ_{47} values are corrected to $\delta^{13}C$, $\delta^{18}O$, and Δ_{47} using the calibration parameters of Brand et al. (2010), following the procedures of Daëron et al. (2016). Raw Δ_{47}values were projected onto the carbon dioxide equilibrium scale and $\delta^{13}C$ and $\delta^{18}O$ values were corrected using the ETH1–3 carbonate standard (Bernasconi et al., 2021). Temperatures were calculated from Δ_{47} values using the calibration of Anderson et al. (2021). Fluid $\delta^{18}O$ values were calculated from calcite $\delta^{18}O$ and Δ_{47}-derived temperatures using the calcite-water oxygen isotope fractionation relationship of Kim and O'Neil (1997). Unless otherwise stated, analytical uncertainties are reported as one standard error (1 SE). Individual analytical uncertainties for $\delta^{13}C$, $\delta^{18}O$, Δ_{47}, temperature, and calculated fluid $\delta^{18}O$ are provided in Table S2 in the Supplement.

4 Results

4.1 Structural characteristics of sampled features at outcrop

Carbonate mineralization sampled in and around Clayton Valley occurs in six principal structural settings: (1) basement-hosted opening-mode veins; (2) basement-hosted faults and fault breccias; (3) basin-bounding normal faults;

(4) volcano-sedimentary basin-fill hosted opening-mode veins; (5) volcano-sedimentary basin-fill hosted faults; and (6) surficial travertine deposits interpreted to record spring systems associated with structurally focused fluid flow at depth. Sampled structures range from cm-scale fractures and veins to fault zones several meters wide and encompass a variety of structural settings, host-rock lithologies, and geographic positions (Figs. 1, 2, and 3).

Basement-hosted opening-mode veins were identified by their relatively planar or tabular geometry, fracture-perpendicular opening displacement, and absence of observable offset of bedding or pre-existing veins and deformation fabrics (Figs. 2a and 3a, b). Sampled opening-mode veins in basement are calcite filled, with measured thicknesses in outcrop of 0.8–8 cm (Table 1). Exposed trace lengths of sampled structures typically range from tens of centimetres to several meters, although the full extent of individual structures was commonly obscured by limited outcrop exposure.

Basement-hosted faults were distinguished by the presence of shear indicators including slickensides and kinematic lineations (e.g., Fig. 2b), fault breccias (Fig. 3c, d), and observed or measurable offset of bedding or pre-existing fabrics (Fig. 3d). Most basement-hosted faults extend beyond the exposed outcrop and lack reliable estimates of total fault dimensions. Similarly, fault displacements for sampled structures are difficult to constrain because offset markers and piercing points were not readily measurable. Basement-hosted faults range from discrete calcite-mineralized fault surfaces (e.g., Fig. 2b) to broader brecciated deformation zones containing abundant calcite cement and fault-filling material (e.g., Fig. 3d).

Two samples were collected from major fault systems developed along the margins of sub-basins within Clayton Valley (Figs. 2c, d and 3e, f). The first sample (CVF1) was collected from the major range-front fault system that defines the eastern margin of Clayton Valley. This fault comprises a relatively broad deformation zone ($\sim$5–10 m) containing multiple overlapping slip surfaces developed within a zone of distributed brittle deformation rather than along a single discrete fault plane (Figs. 2c and 3e). Calcite mineralization occurs along individual slip surfaces and within localized fault-core breccias (Fig. 2c), and alluvial-fan deposits are preserved directly adjacent to the fault zone and are themselves deformed and displaced by faulting (Fig. 3e), indicating continued fault movement following fan deposition and prolonged fault activity along the basin-margin fault system. The second sample from a major mapped fault (CVF3) was collected from the western margin of Angel Island (Fig. 1). This fault juxtaposes basin-fill deposits against basement rocks and forms a structural boundary between the Angel Island basement high to the east and the adjacent sedimentary basin fill to the west (Figs. 1, 2d, and 3f). Calcite mineralization occurs in dilational jogs along a slickensided slip surface. Earlier calcite veins within the basement are crosscut and offset by the principal slip surface, and late-stage calcite mineralization coats the slip surface itself (Fig. 3f). This younger calcite generation is kinematically compatible with mineralization associated with fault slip, and was targeted for U–Pb geochronology and geochemical analyses.

Opening-mode veins hosted within volcano-sedimentary basin-fill deposits occur primarily within ash-rich volcaniclastic, lacustrine, and volcano-sedimentary strata (Fig. 3g, h). Observed vein apertures range from approximately 0.3 to 2 cm, and exposed trace lengths range from approximately 1 to 5 m. The full extent of individual veins is commonly obscured by limited outcrop exposure. Several veins preserve bladed calcite fabrics and subtle internal banding or medial seams that may reflect repeated episodes of fracture opening and calcite precipitation (Fig. 3g, h).

Faults hosted within volcano-sedimentary basin-fill deposits range from discrete calcite-mineralized faults with measurable offsets to broad brecciated fault zones several meters wide (Table 1). Calcite mineralization occurs along slip surfaces and within localized dilational zones (Figs. 2e and 3i). Measured displacements range from 23 to 46 cm where observable, although the full dimensions and cumulative displacements of many structures are difficult to constrain because fault traces commonly extend beyond the limits of outcrop exposure.

Travertine samples were collected from spring-related carbonate deposits exposed at the surface (Fig. 2f; Tables S1 and S2). These deposits range from dense, banded travertines to highly porous carbonate accumulations and preserve characteristic layering and precipitation fabrics associated with near-surface fluid discharge.

4.2 Calcite petrography and microstructures

To facilitate comparison between samples, calcite fabrics were grouped into seven petrographic classes based on crystal morphology, texture, and structural relationships (Table 1). Crystal size and morphology follow the terminology of Folk (1959, 1962, 1965), and interpretations of vein growth textures and fault-related calcite fabrics draw on established concepts for vein microstructures and fracture-fill evolution (e.g., Bons et al., 2012; Roberts and Holdsworth, 2022). The classification scheme presented here was developed specifically for this study and is intended as a practical framework for comparing calcite fabrics across the range of sampled structures. Fabric classes comprise: (1) crack-seal calcite; (2) bladed, syntaxial, and antitaxial calcite; (3) equant to blocky medium- to coarsely crystalline calcite; (4) fine- to microcrystalline calcite; (5) botryoidal, radial, and travertine-like calcite; (6) slickensided calcite fill; and (7) breccia cement. Multiple fabric classes may be assigned to individual samples where more than one calcite fabric is present.

Petrographic observations show substantial textural variability within carbonate-bearing structures (Fig. 4). Most samples contain multiple texturally distinct calcite domains

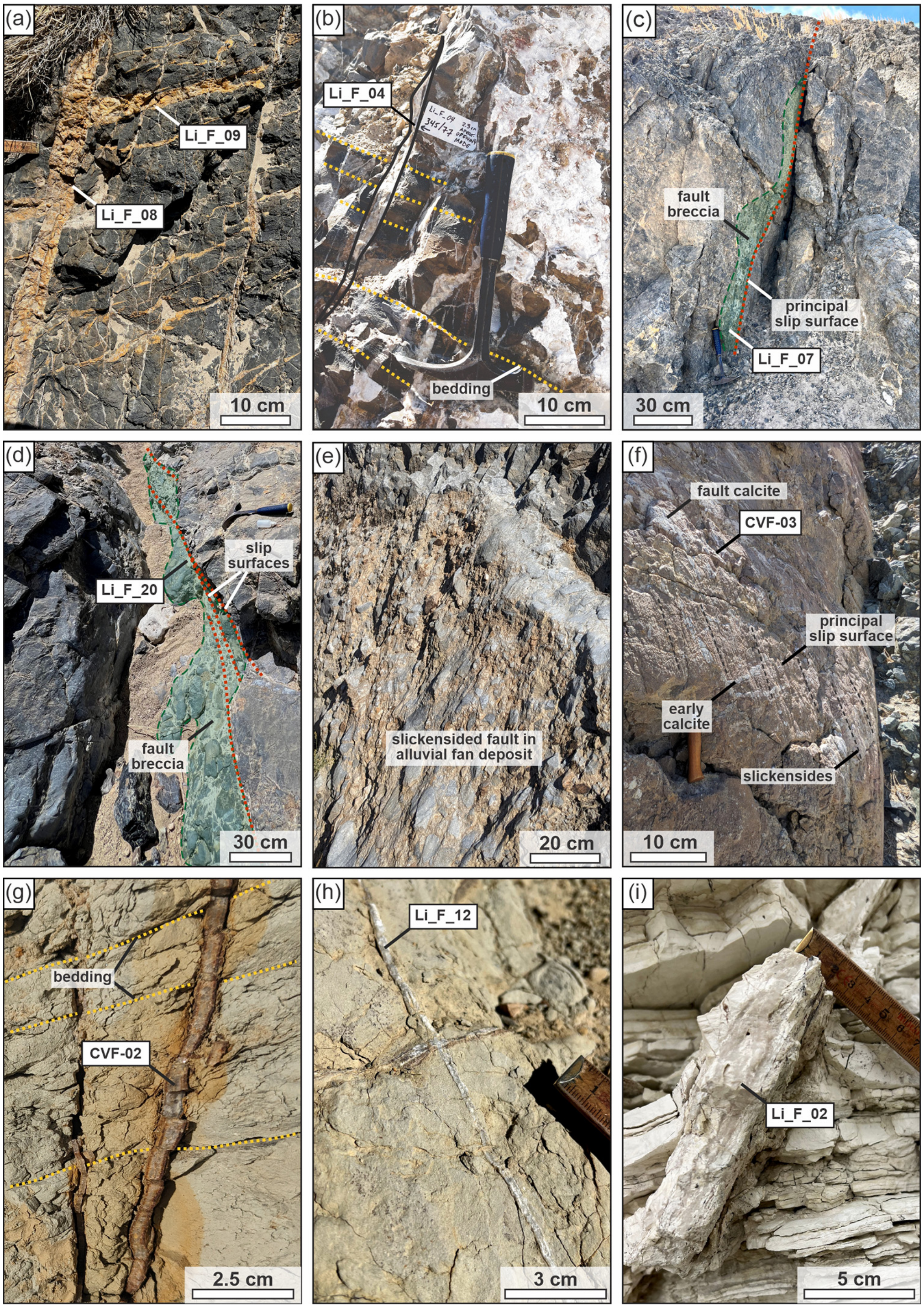

Figure 3. Representative field photographs of structures sampled for U–Pb geochronology and geochemical analyses. **(a, b)** Basement-hosted opening-mode veins. **(c, d)** Basement-hosted faults and associated mineralization. **(e, f)** Basin-bounding and major basin-margin faults (see Fig. 2c and d for context). **(g, h)** Opening-mode veins hosted within basin-fill deposits. **(i)** Basin-fill-hosted normal fault (see Fig. 2e for context). Yellow dotted lines indicate bedding, red dotted lines indicate slip surfaces, and the black dashed line in panel **(f)** shows observed slickenlines. These structures record a range of deformation styles and fluid-flow pathways within basement, basin-margin, and basin-fill settings across the study area. See main text for additional details of the sampled structures and their geological context.

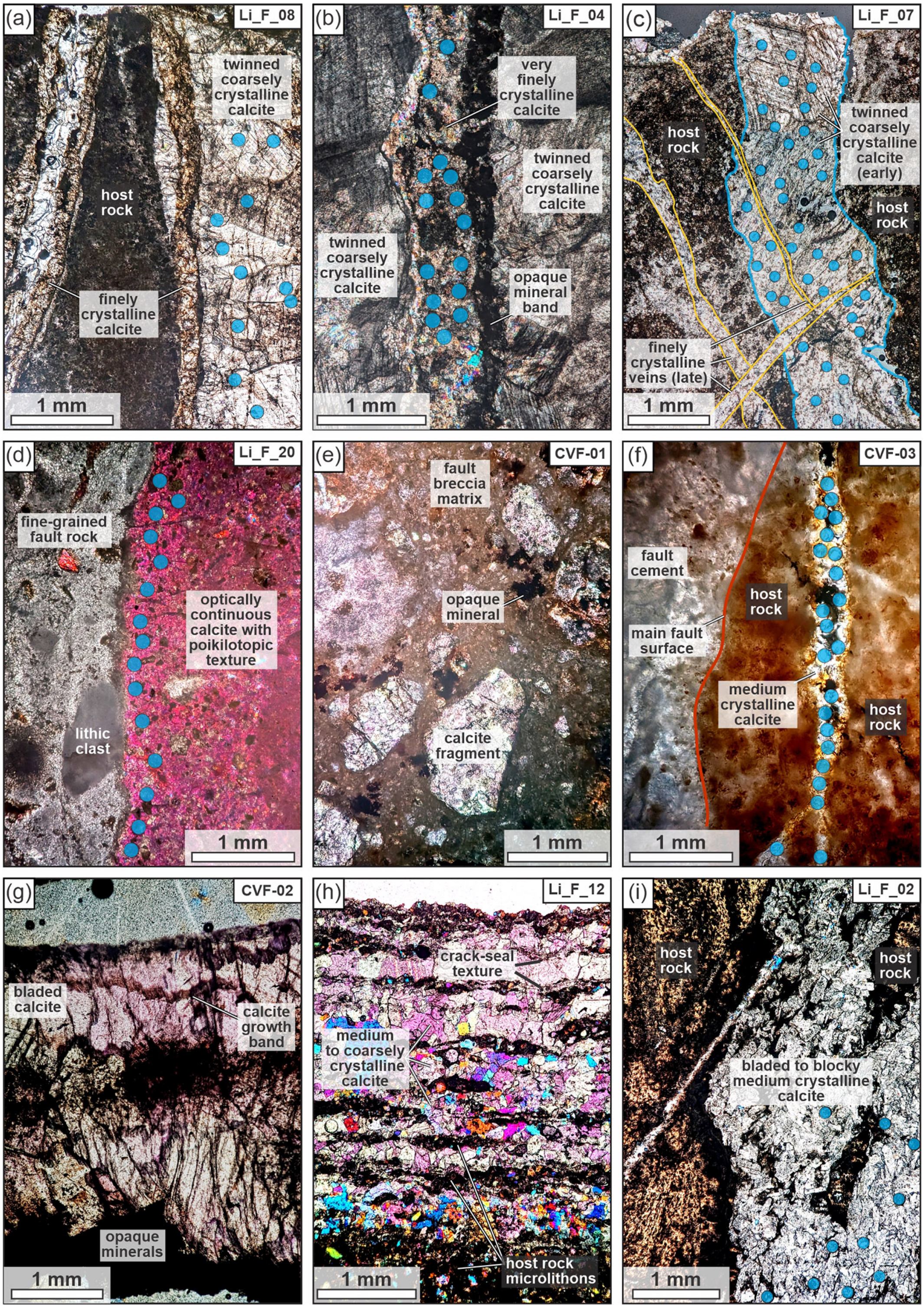

Figure 4. Representative petrographic images of sampled structures. Panels **(a)**–**(i)** correspond directly to the field photographs shown in Fig. 3. **(a, b)** Basement-hosted opening-mode veins. **(c, d)** Basement-hosted faults and associated mineralization. **(e, f)** Basin-bounding and major basin-margin faults. **(g, h)** Opening-mode veins hosted within basin-fill deposits. **(i)** Basin-fill-hosted normal fault. Blue circles indicate laser ablation U–Pb spot locations. In the examples shown, laser ablation analyses were targeted within texturally distinct calcite domains to minimize sampling across multiple generations of calcite growth. See main text for descriptions of petrographic textures and calcite paragenesis.

Table 1. Summary of sampled structures.

Sample ID	Setting	Structure	Sampled vein thickness	Calcite Fabric Class
CVF-4	Basement	Opening-mode vein	~ 4 cm	5
CVF-5	Basement	Opening-mode vein	~ 3.5 cm	3, 4, 7
CVF-6	Basement	Opening-mode vein	~ 8 cm	3, 5
Li_F_04	Basement	Opening-mode vein	~ 2.3 cm	3, 4
Li_F_05	Basement	Opening-mode vein	~ 1 cm	3
Li_F_08	Basement	Opening-mode vein	~ 4.3 cm	3, 4
Li_F_09	Basement	Opening-mode vein	~ 2.6 cm	1, 2, 3
Li_F_10	Basement	Opening-mode vein	~ 2.8 cm	3
Li_F_19	Basement	Opening-mode vein	~ 0.8 cm	2, 3, 4
Li_F_01	Basement	Dilational normal fault	~ 6 cm	3, 4
Li_F_06	Basement	Dilational normal fault	~ 4 cm	3
Li_F_07	Basement	Fault breccia adjacent to slip surface	~ 12 cm	3, 4, 7
Li_F_17	Basement	Fault breccia zone	~ 14 cm	3, 4, 7
Li_F_18	Basement	Normal fault	~ 0.5 cm	1, 3, 4, 6
Li_F_20	Basement	Fault breccia zone (~ 30 cm wide)	~ 4 cm	4, 6
CVF-1	Basin-bounding fault	Normal fault, mineralized breccia	~ 1.2 cm	4, 6, 7
CVF-3	Basin-bounding fault	Normal fault	~ 0.8 cm	3, 6
CVF-2	Volcano-sedimentary	Opening-mode vein	~ 0.5 cm	2
Li_F_11	Volcano-sedimentary	Opening-mode vein	~ 2 cm	3, 4
Li_F_12	Volcano-sedimentary	Opening-mode vein	~ 0.3 cm	1, 3
Li_F_15	Volcano-sedimentary	Opening-mode vein	~ 0.7 cm	3, 4
Li_F_16	Volcano-sedimentary	Opening-mode vein	~ 0.9 cm	3, 4
Li_F_02	Volcano-sedimentary	Dilational normal fault	~ 2 cm	4
Li_F_03	Volcano-sedimentary	Normal fault	~ 0.15 cm	2, 3, 4
Li_F_13	Volcano-sedimentary	Strike-slip fault zone (~ 2 m wide)	~ 2 cm	2, 4
Li_F_14	Volcano-sedimentary	Strike-slip fault zone (~ 2 m wide)	~ 0.5 cm	3, 4

Paleo-spring travertine samples were not petrographically classified and are not included in the table. Calcite fabric classes are described in the main text.

separated by sharp contacts, opaque seams, growth bands, or crosscutting relationships. Crosscutting and abutting vein relationships, brecciation and recementation textures, crack-seal fabrics, and multiple generations of calcite growth indicate that some sampled structures record repeated episodes of fracturing, fluid flow, and calcite precipitation. Where multiple calcite generations were present, LA-ICP-MS analyses were targeted to petrographically coherent calcite domains and avoided sampling spots from different crosscutting zones, vein margins, host-rock inclusions, and texturally distinct calcite generations where possible (Fig. 4).

Basement-hosted opening-mode veins commonly contain multiple calcite fabrics within individual veins (Fig. 4a, b). Finely crystalline calcite, medium- to coarsely crystalline calcite, and inclusion-rich calcite domains occur adjacent to one another and are separated by sharp contacts, dark seams, or discrete growth bands. Distinct calcite fabrics commonly define subparallel bands or lenses within individual veins, likely indicating multiple episodes of calcite growth and vein evolution.

Basement-hosted faults and fault breccias preserve a range of calcite fabrics and structural relationships (Figs. 4c, d, and S1). Some samples contain multiple generations of calcite veins and fracture fills that crosscut one another, with fine-crystalline calcite cutting across earlier coarsely crystalline calcite domains (Fig. 4c). Other samples are dominated by relatively homogeneous fault-fill calcite characterized by fine- to microcrystalline fabrics and abundant dark inclusion-rich material (Fig. 4d). Additional basement-hosted fault samples preserve coarsely crystalline twinned calcite, equant mosaic textures, and multiple calcite fabrics separated by dark seams and growth bands (Tables 1 and S1).

Basin-bounding faults preserve calcite fabrics distinct from those observed in many basement-hosted structures. CVF-01 comprises a mineralized fault breccia containing angular to subangular calcite clasts supported by a fault breccia matrix (Fig. 4e). Sample CVF-03 preserves a medium-crystalline calcite vein adjacent to the principal slip surface (Fig. 4e). Earlier calcite veins are crosscut and offset by both the principal slip surface and the sampled vein. The sampled vein has a similar orientation to the principal slip surface and is interpreted to be associated with a later phase of fault-related calcite mineralization.

Opening-mode veins hosted within volcano-sedimentary basin-fill deposits commonly preserve growth fabrics indicative of repeated fracture opening and calcite precipitation, including bladed calcite and growth banding (Fig. 4g), and crack-seal textures (Fig. 4h). Calcite within basin-fill-hosted faults ranges from fine-crystalline fault-fill material developed along discrete slip surfaces to bladed and blocky calcite within localized dilational zones (Fig. 4i). Several samples preserve evidence for multiple generations of mineralization and fault reactivation, including crosscutting calcite fabrics and brecciation. The full suite of petrographic images is provided in Fig. S1.

4.3 Lithium concentrations

Measured lithium concentrations in fault- and fracture-hosted calcite veins and spring deposit carbonates range from below detection limits (< 2 ppm; ALS, 2025) to 460 ppm (Figs. 5a, 6a, and 7). Four of the 30 samples analyzed yielded lithium concentrations below detection limits, all of which are fault- and fracture-hosted samples within Proterozoic to Paleozoic basement units (Table 2). For basement-hosted faults and fractures with measurable lithium, concentrations range from 3 to 29 ppm (median = 6 ppm; $n = 11$). Calcite veins in volcano-sedimentary basin-fill units exhibit the greatest variability in lithium concentrations, ranging from 3 to 460 ppm (median = 16 ppm; $n = 9$). Travertine and spring deposits yield consistently elevated lithium concentrations (13 to 112 ppm; median = 68.5 ppm; $n = 4$) relative to most vein calcites. Samples from basin-bounding faults contain comparatively low lithium concentrations (6–12 ppm; median = 9 ppm; $n = 2$). The full suite of bulk geochemistry data is provided in Table S2.

4.4 U–Pb calcite ages

A total of 26 calcite samples were analyzed by LA-ICP-MS U–Pb geochronology, of which 13 yielded interpretable ages (Table 2). Prior to analysis, reconnaissance spot analyses were used to identify calcite domains with elevated U / Pb ratios and limited common Pb, and U–Pb analyses were subsequently targeted toward these domains where possible. Despite this screening approach, many samples contained insufficient radiogenic Pb, elevated common Pb, or a combination of both, precluding robust age determination. Uncertainties associated with the resulting ages vary substantially, reflecting differences in U / Pb ratios and common Pb contents among samples. Where multiple calcite fabrics or generations were present within a sample, U–Pb analyses were targeted to petrographically coherent calcite domains and, where possible, confined to individual growth zones or texturally distinct calcite generations (Fig. 4). Although petrographic complexity is present in several samples, the analyses retained for age calculation define internally coherent Tera-Wasserburg regression arrays, supporting interpretation of the dated domains as isotopically consistent calcite populations (Fig. S2).

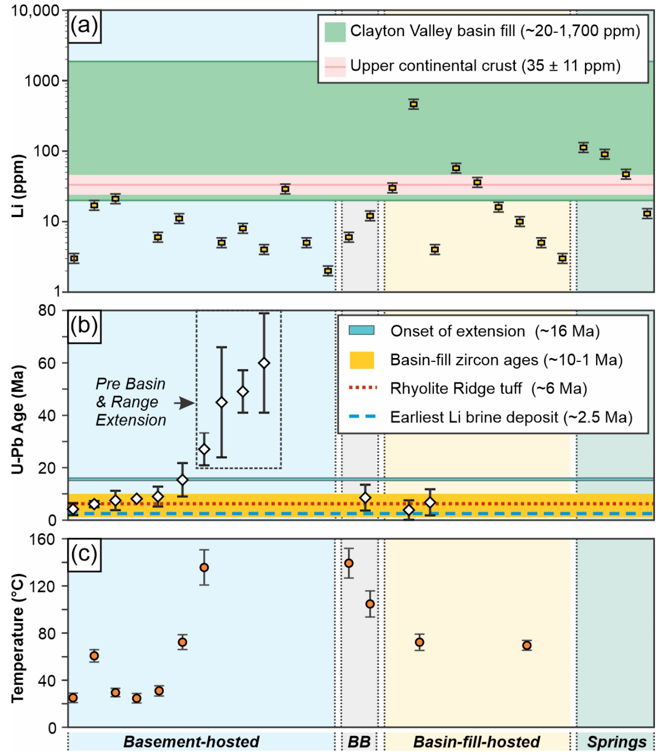

Figure 5. Geochemical data for calcite veins and travertine spring deposits. **(a)** Lithium concentrations (ppm); vertical error bars represent ±10 % analytical uncertainty (ALS, 2025). The dark pink horizontal reference bar shows average upper continental crust lithium concentration of 35 ppm from Teng et al. (2004), and the light pink band shows the reported ±11 ppm uncertainty, corresponding to 24–46 ppm. The horizontal green bar shows lithium concentrations for basin-fill sediments from Coffey et al., 2021. **(b)** U–Pb calcite ages (Ma); vertical error bars indicate 2σ uncertainty. Horizontal bars indicate onset of Basin and Range extension in the Clayton Valley-Silver Peak region (Diamond and Ingersoll, 2002), basin-fill zircon ages (Rangel et al., 2025), the Rhyolite Ridge tuff (Darin et al., 2025), and earliest halite deposition in Clayton Valley (Coffey et al., 2021; Gagnon et al., 2023). Ages older than the onset of Basin and Range extension (∼ 25 Ma; Stewart, 1998) are highlighted. **(c)** Clumped-isotope temperatures (°C); vertical error bars represent 1σ uncertainty. Shaded vertical bands in panels **(a)**–**(c)** indicate sample setting; BB = basin-bounding faults.

U–Pb ages obtained from calcite mineralization span from 60 ± 19 to 3.9 ± 3.7 Ma (Figs. 5b, 6b, and 7). Calcite mineralization hosted in faults and fractures within Proterozoic to Paleozoic basement rocks records the broadest range of ages, from 60 ± 19 to 4.2 ± 2.3 Ma. The basin-bounding fault west of Angel Island (Fig. 2d) yields an age of 8.6 ± 4.9 Ma (Fig. 5). Veins hosted in volcano-sedimentary basin-fill units generally record younger ages, from 6.8 ± 5.0 to 3.9 ± 3.7 Ma (Table 2). Several calcite samples did not yield robust U–Pb ages due to high proportions of common Pb. Travertine and spring deposits were not analyzed for U–Pb geochronology. U–Pb calcite geochronology data and as-

Table 2. Summary of samples and analytical results, ordered by setting. Full dataset provided in Table S2.

ID	Li (ppm)	U–Pb Age (Ma)	± Age uncertainty (2SE)	δ^{13}C VPDB (‰)	δ^{18}O VPDB (‰)	δ^{18}O VSMOW (‰)	Δ_{47} (I-CDES, ‰)	Temp. (°C)	± Temp. 1 SE (°C)	δ^{18}Owater VSMOW (‰)
CVF-4	3	4.2	2.3	1.25	−13.77	16.73	0.59	24.95	4.07	−11.41
CVF−5	21	7.5	3.7	−0.18	−15.06	15.39	0.58	29.45	3.54	−11.82
CVF−6	< 2	8.2	0.3	−1.22	−13.91	16.58	0.60	24.61	4.05	−11.62
Li_F_04	8	49.1*	8.1	−0.61	−13.16	17.36	–	–	–	–
Li_F_05	< 2	–	–	–	–	–	–	–	–	–
Li_F_08	5	45*	21.0	−0.06	−25.24	4.90	–	–	–	–
Li_F_09	4	60*	19.0	0.17	−16.13	14.29	–	–	–	–
Li_F_10	5	–	–	–	–	–	–	–	–	–
Li_F_19	29	–	–	–	–	–	–	–	–	–
Li_F_01	2	–	–	–	–	–	–	–	–	–
Li_F_06	11	15.4	6.4	0.34	−18.77	11.57	0.48	72.25	6.33	−8.24
Li_F_07	6	9.0	3.8	0.22	−16.59	13.82	0.58	30.88	4.31	−13.07
Li_F_17	< 2	–	–	–	–	–	–	–	–	–
Li_F_18	< 2	27.1*	6.2	−0.21	−12.66	17.87	0.39	135.62	14.90	6.04
Li_F_20	17	6.1	1.2	−0.97	−14.71	15.75	0.51	60.61	5.23	−5.96
CVF−1	12	–	–	−0.98	−22.68	7.54	0.43	104.61	11.05	−7.77
CVF−3	6	8.6	4.9	−1.02	−21.84	8.40	0.38	139.16	12.58	−2.94
CVF−2	10	–	–	−0.57	−18.98	11.35	0.49	69.51	4.12	−8.87
Li_F_11	4	–	–	0.59	−22.18	8.06	–	–	–	–
Li_F_12	16	–	–	–	–	–	–	–	–	–
Li_F_15	3	–	–	–	–	–	–	–	–	–
Li_F_16	36	–	–	−3.8	−29.6	0.4	–	–	–	–
Li_F_02	460	6.8	5.0	3.43	−7.41	23.28	0.48	72.11	6.85	3.22
Li_F_03	30	3.9	3.7	–	–	–	–	–	–	–
Li_F_13	57	–	–	−2.91	−31.80	−1.86	–	–	–	–
Li_F_14	5	–	–	–	–	–	–	–	–	–

* U–Pb ages older than 25 Ma are interpreted to pre-date Basin and Range extension in study area. See main text for details.

sociated Tera–Wasserburg plots are provided in Table S3 and Fig. S2.

4.5 Stable isotope and clumped-isotope geochemistry

Clumped-isotope (Δ_{47}) and stable isotope analyses were performed on a subset of fault- and fracture-hosted calcite samples, including vein calcite and travertine deposits (Figs. 5c, 6c, and 7). Measured Δ_{47} values range from 0.384 ± 0.014 ‰ to 0.595 ± 0.012 ‰, corresponding to temperatures of 24.6 ± 4.1 to 139.2 ± 12.6 °C. Reconstructed fluid δ^{18}O values were calculated from measured calcite δ^{18}O and Δ_{47}-derived temperatures using the calcite-water oxygen isotope fractionation relationship of Kim and O'Neil (1997). Reconstructed carbonate precipitation temperatures span from 25 to 139 °C across the dataset (Table 2). Calcite hosted on basin-bounding faults records two elevated temperatures of 104.6 and 139.2 °C. The two volcano-sedimentary samples analyzed by clumped-isotope thermometry yield similar precipitation temperatures of 69.5 and 72.1 °C. Calcite mineralization hosted in basement faults and fractures spans the widest range of temperatures, with low-temperature values of 25–31 °C, intermediate values of 60.6 and 72.3 °C, and a high-temperature value of 135.6 °C. Carbonate δ^{13}C values range from −3.8 to +3.4 ‰ (VPDB), and carbonate δ^{18}O values range from −31.8 ‰ to −7.4 ‰ (VPDB). Calculated fluid δ^{18}O values range from −13.1 ‰ to +6.0 ‰ (VSMOW) over Δ_{47} temperatures of 24.6–139.2 °C, with dashed contours indicating equilibrium calcite δ^{18}O compositions (Fig. 8a). Clumped-isotope formation temperatures generally increase with U–Pb calcite age, with older calcite generations tending to record higher precipitation temperatures (Fig. 8b). Stable isotope and clumped-isotope data, including Δ_{47} measurements and calculated fluid compositions, are provided in Table S4.

5 Discussion

5.1 Veins and spring deposits as tracers of lithium transport

Calcite veins and travertine spring deposits sampled here provide direct records of fluid chemistry at the time of mineralization (Fyfe et al., 1978; Eaton, 1982; Chen et al., 2024).

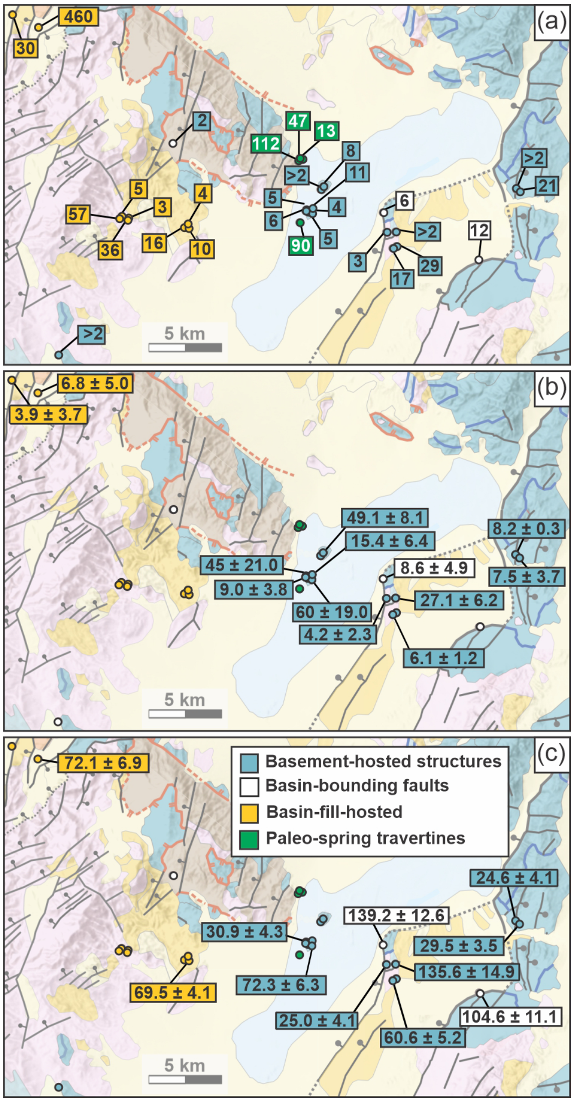

Figure 6. Spatial distribution of geochemical and geochronologic data from calcite veins and travertine deposits in and around Clayton Valley, Nevada. **(a)** Lithium concentrations in calcite (ppm). **(b)** U–Pb calcite ages (Ma). **(c)** Clumped-isotope calcite precipitation temperatures (°C). Symbols are color-coded by host setting (legend in panel **a**). Numeric labels indicate measured values for individual samples. See Fig. 1 for larger geologic context. These spatial data correspond to summary distributions presented in Fig. 5.

These samples document lithium mobilization and transport by fluids circulating along faults and fractures in and around a basin that hosts one of the world's largest lithium accumulations (24–58 Mt; Coffey et al., 2021). Most samples contain measurable lithium, indicating that lithium was present in solution during fault- and fracture-hosted fluid flow at the time of vein and travertine formation. Lithium concentrations are highest and most variable within volcano-sedimentary basin-fill units, including the highest measured value of 460 ppm, and paleo-spring travertine deposits also yield relatively elevated concentrations (13–112 ppm). Most reconstructed fluid compositions are consistent with dominantly meteoric waters (δ^{18}Owater ≈ -13 ‰ to -6 ‰ VSMOW). The highest Li concentration (460 ppm), however, occurs in a sample that yields a substantially heavier reconstructed fluid composition ($\sim +3$ ‰ VSMOW), suggesting that the most Li-enriched fluid may have involved a greater contribution from evolved basin fluids or more extensive water-rock interaction than the majority of the dataset. In contrast, basement-hosted structures contain lower lithium concentrations, with four samples below analytical detection limits (< 2 ppm) and the remaining samples ranging from 2 to 29 ppm. Basin-bounding fault samples contain similarly low lithium concentrations (6 and 12 ppm).

Many of the calcite veins analyzed here contain relatively low lithium concentrations compared to the average upper continental crust abundance of 35 ± 11 ppm reported by Teng et al. (2004), particularly within basement-hosted and basin-bounding structures. Interpretation of calcite lithium concentrations is not straightforward because lithium incorporation into calcite is strongly partition-limited and depends on fluid lithium/calcium ratios, growth conditions, temperature, pH, and fluid chemistry rather than dissolved lithium concentration alone. Experimental and natural-system studies demonstrate substantial variability in calcite-fluid lithium partition coefficients (e.g., Füger et al., 2019; Drake et al., 2018; Branson et al., 2024), indicating that relatively low lithium concentrations in calcite do not necessarily imply lithium-poor parent fluids. This issue is particularly important when comparing calcite lithium concentrations to bulk upper continental crust compositions, which are dominated by silicate- and clay-rich lithologies (Teng et al., 2004) that are substantially more favourable hosts for lithium than calcite.

To evaluate whether the observed calcite lithium concentrations are compatible with precipitation from lithium-bearing basin fluids, we performed a simple forward-modeling exercise using modern Clayton Valley brine compositions reported by Coffey et al. (2021). We calculated fluid lithium/calcium ratios for modern Clayton Valley waters and propagated these ratios through experimentally derived calcite-fluid partition coefficients reported by Füger et al. (2019), Drake et al. (2018), and Branson et al. (2024). Predicted calcite lithium distributions vary substantially depending on the partition coefficient employed. Of the partitioning scenarios evaluated, only the intermediate partition coefficients of Füger et al. (2019) produce predicted calcite Li distributions that compare closely with the observed dataset, whereas the remaining scenarios show only partial overlap (Sect. S1, Table S5, Figs. S3 and S4). Although we do not infer that these partition coefficients are uniquely applicable to the Clayton Valley system, they provide the closest correspondence with the observed dataset among the published partitioning relationships evaluated. We do not interpret this correspondence to mean that the intermediate Füger et al. (2019) partition coefficients uniquely describe the Clayton

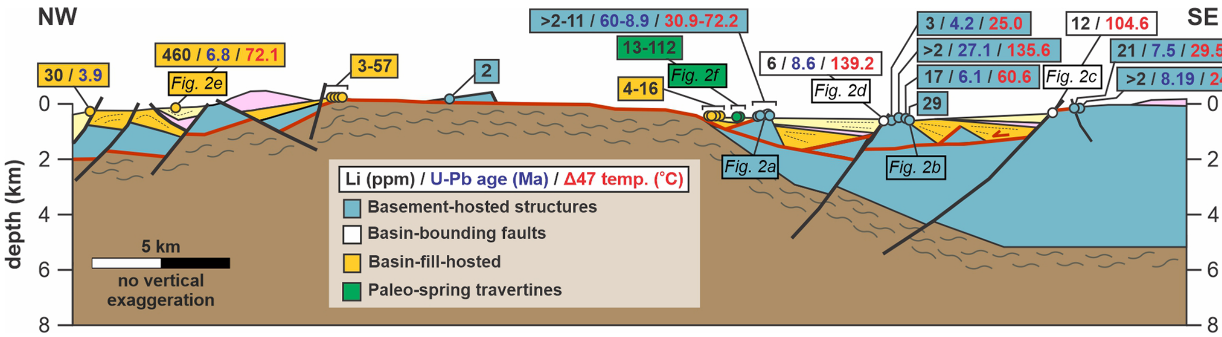

Figure 7. NW-SE cross section across study area (location shown in Fig. 1) showing projected sample locations and lithium concentrations, U–Pb ages, and clumped isotope temperatures. Modified from Cawood et al. (2025) and Rangel et al. (2025). Analytical uncertainties are omitted for clarity (see Fig. 5 and Table S2 for full suite of data and uncertainties).

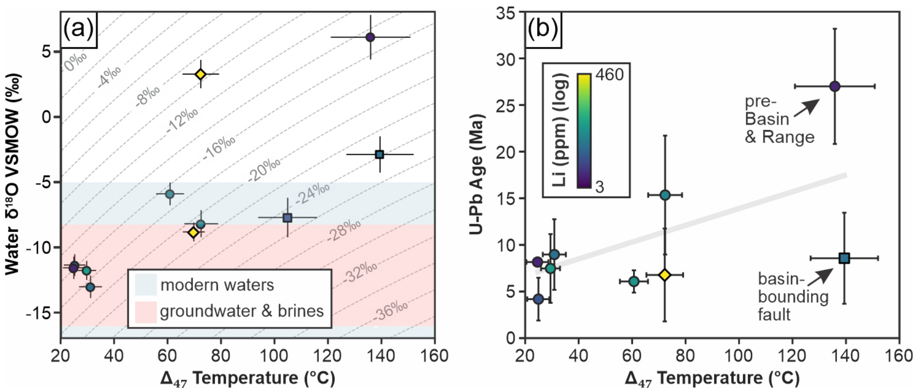

Figure 8. (a) Reconstructed fluid $\delta^{18}O$ (VSMOW) versus Δ_{47} temperature. Dashed contours show equilibrium calcite $\delta^{18}O$ (VPDB) calculated using the fractionation relationship of Kim and O'Neil (1997). Shaded fields show representative ranges of modern meteoric recharge and groundwater/brines for Clayton Valley (Gagnon et al., 2023). **(b)** U–Pb calcite age versus clumped-isotope temperature. Symbols in both panels indicate structural setting (circles = basement-hosted structures; diamonds = basin-fill–hosted structures; squares = basin-bounding faults). Symbol colours indicate calcite lithium concentration.

Valley system. Rather, it demonstrates that published, experimentally derived partitioning relationships are capable of reproducing the observed calcite Li concentrations under plausible conditions. As demonstrated by Füger et al. (2019), Li partitioning in calcite is highly sensitive to growth rate and pH, and we lack independent constraints on these variables for the natural samples. Future work should evaluate these controls more directly to refine partitioning relationships for natural hydrothermal systems. These calculations show that calcite containing only ppm- to tens-of-ppm lithium is potentially compatible with precipitation from lithium-bearing basin fluids and that relatively low calcite lithium concentrations do not necessarily imply lithium-poor parent fluids.

We emphasize that this analysis is not intended as a formal reconstruction of paleo-fluid compositions. Partition coefficients likely varied among individual veins as a function of evolving fluid chemistry, precipitation conditions, temperature, and growth rate, and modern Clayton Valley brines may not be representative of all paleo-fluid compositions present during basin evolution. Rather, this forward-modeling exercise provides a first-order test of whether the observed calcite lithium concentrations are geochemically compatible with precipitation from lithium-bearing basin fluids. The results indicate that they are. Consequently, the calcite lithium dataset presented here should not be interpreted as a direct quantitative reconstruction of paleo-fluid lithium concentrations or as evidence for uniformly lithium-rich fluids throughout basin evolution. Instead, the data indicate variable interaction between structurally focused fluids and lithium-bearing basin materials, with faults and fracture networks acting as pathways that facilitated fluid circulation, fluid-rock interaction, and localized redistribution of lithium during basin development. Accordingly, these calculations should be regarded as illustrative rather than as reconstructions of pre-6 Ma fluid chemistry.

5.2 Timing and sources of lithium-bearing fluids

Vein calcite precipitation ages span ∼ 60 to 3.9 Ma, with the majority of ages associated with Basin and Range extension and basin development falling between ∼ 15.4 and 3.9 Ma (Figs. 5, 6, and 7). These ages suggest that lithium-bearing fluids were present both before and during Basin and Range deformation and basin development, rather than being restricted to a single episode of fluid flow and mineralization. Calcite ages associated with Basin and Range extension (∼ 15.4 and 3.9 Ma) overlap both early activity of the Silver Peak–Lone Mountain detachment system (∼ 16–6 Ma; Oldow et al., 1994, 2008) and later phases of deformation associated with development of the modern basin geometry (∼ 6 Ma and younger; Rangel et al., 2025), highlighting the longevity of structurally controlled fluid pathways during basin evolution (Fig. 9).

Previous studies have identified lithium-rich silicic volcanic rocks of the Montezuma Range as the major source for lithium within the basin (Price et al., 2000), and more recent work has demonstrated that the Rhyolite Ridge tuff, which hosts the lithium-boron mineralization at Rhyolite Ridge and the Cave Spring Basin NW of Clayton Valley, is geochemically and temporally linked to volcanic units exposed in the Montezuma Range and may represent part of the same regional volcanic system (Darin et al., 2025). Late Miocene silicic volcanism therefore likely represents the dominant source for lithium brine and volcano-sedimentary deposits in the Clayton Valley area. Five calcite veins yield U–Pb ages with 95 % confidence intervals (reported as 2σ uncertainties) that pre-date emplacement of the ∼ 6.05 Ma Rhyolite Ridge Tuff (Table 2). Although lithium concentrations in these samples are modest (< 2–11 ppm), consideration of published calcite-fluid lithium partition coefficients together with modern Clayton Valley brine compositions (Sects. 5.1 and S1) demonstrates that calcite containing only ppm- to tens-of-ppm lithium may plausibly precipitate from lithium-enriched fluids owing to the strongly partition-limited and highly variable incorporation of lithium into calcite. Consequently, these older calcites cannot be assumed to record lithium-poor parent fluids based solely on their absolute lithium concentrations. Nevertheless, the highest lithium concentrations measured in this study are associated with younger basin-fill and fault systems that are contemporaneous with, or post-date, emplacement of the late Miocene silicic volcanic units.

Potential lithium reservoirs that pre-date emplacement of the late Miocene silicic volcanic units may include Jurassic to Tertiary granitic rocks exposed throughout the ranges surrounding Clayton Valley, including the Palmetto Mountains south of the basin, the Weepah Hills and Lone Mountain to the north, and smaller exposures at Mineral Ridge (Albers and Stewart, 1972; Price et al., 2000). Lithium-bearing pegmatites containing lepidolite have also been reported from Mineral Ridge (Bailly, 1951; Olson and Hinrichs, 1960; Albers and Stewart, 1972), though Papke (1976) rejected these pegmatites as a major lithium source in the area because of the small amount of material exposed. Regional models have also invoked long-range groundwater circulation as a potential mechanism for mobilizing and transporting lithium across basin systems (e.g., Munk et al., 2016), highlighting the potential for lithium sourcing from pre-6 Ma igneous or volcano-sedimentary materials adjacent to Clayton Valley. Although our calcite dataset is better suited to evaluating the timing, temperatures, and pathways of lithium-bearing fluid circulation than to uniquely identifying lithium sources, these older local and regional reservoirs remain plausible hypotheses that warrant further investigation.

5.3 Fluid circulation recorded by clumped and stable isotopes

Clumped-isotope temperatures record pronounced variability in the thermal conditions of calcite precipitation across structural settings in Clayton Valley (Figs. 5–7). Calcite mineralization along basin-bounding faults records the highest precipitation temperatures (139.2 and 104.6 °C), consistent with deep circulation along major fault systems. A similarly elevated temperature (135.6 °C) recorded by a basement-hosted vein is interpreted to reflect hydraulic connectivity to the basin-bounding fault system at depth. Calcite veins hosted in volcano–sedimentary units yield tightly clustered intermediate temperatures (∼ 70 °C), whereas basement-hosted structures span the widest temperature range, from near-ambient (∼ 20–31 °C) to the highest recorded values.

A schematic structural evolution model for the area provides a framework for evaluating the relationship between calcite precipitation temperatures, structural position, and basin evolution (Fig. 10). The oldest calcite vein associated with Basin and Range deformation (15.4 ± 6.4 Ma) records an intermediate precipitation temperature of 72.3 °C and formed during the early stages of regional extension (Fig. 10a). Regional reconstructions indicate that extension along the Silver Peak–Lone Mountain detachment system was underway by this time (e.g., Oldow et al., 1994, 2008). Thermochronology constraints indicate that Mineral Ridge may have been exhumed to ∼ 3.5 km depth by 11 Ma (Oldow et al., 1994), suggesting that substantial crustal attenuation and associated exhumation of Mineral Ridge had already occurred by this time. The normal fault-hosted 15.4 Ma calcite sample likely records mineralization associated with fluid circulation through structurally focused pathways during an interval of active extension, crustal attenuation, and elevated geothermal gradients.

By ∼ 6 Ma, restored basin geometries indicate that multiple generations of calcite veins had already formed and record a wide range of precipitation temperatures (Fig. 10b). Near-ambient precipitation temperatures are strongly suggestive of shallow, meteoric-derived fluids. This interpretation is reinforced by sequential structural restoration of Clayton Valley, which places several low-temperature, lithium-bearing calcite veins at or near the Earth's surface at the time of mineralization. In contrast, coeval calcite veins that record higher temperatures occur on basin-bounding or subsidiary faults. This pattern suggests that some structures were

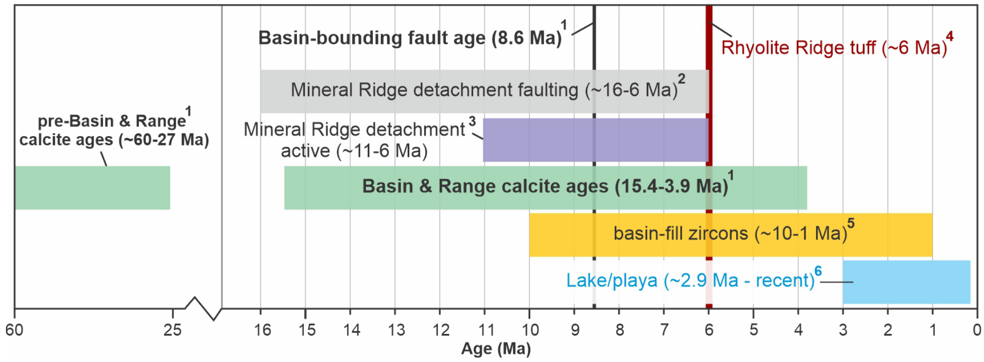

Figure 9. Time plot of U–Pb calcite ages from this study and published constraints on regional tectonic, volcanic, and basin evolution. Data sources (superscripts): 1 – this study; 2 – Diamond and Ingersoll (2002); 3 – Oldow et al. (1994); 4 – Darin et al. (2025); 5 – Rangel et al. (2025); 6 – Coffey et al. (2021) and Gagnon et al. (2023).

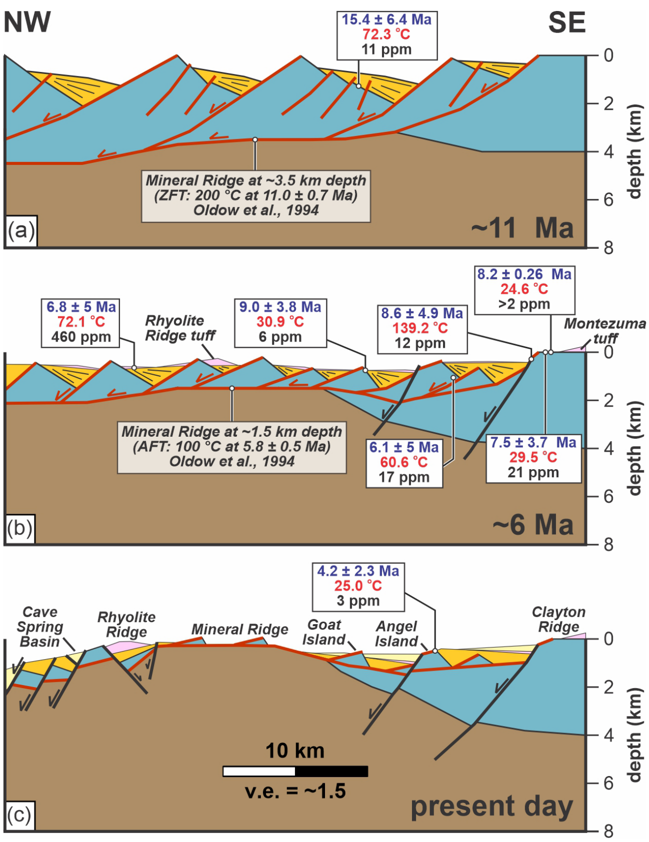

Figure 10. Schematic structural evolution of Clayton Valley at **(a)** ∼ 11 Ma, **(b)** ∼ 6 Ma, and **(c)** present-day. Vein calcite sample ages (blue), temperatures (red), and lithium concentrations (black) are shown relative to the evolving basin architecture. Samples are plotted at approximate time intervals when they are interpreted, based on U–Pb ages, to have already been present; panels do not imply fault initiation or mineralization at the illustrated times. Approximate paleodepth estimates for Mineral Ridge at ca. 6 and ca. 11 Ma are based on published apatite and zircon fission-track constraints from Oldow et al. (1994) and assume an elevated geothermal gradient of 50 °C km^{-1} associated with regional extension and crustal thinning.

connected to deeper circulation levels, indicating mineralization associated with shallow meteoric and deeper hydrothermal fluids occurred contemporaneously (Fig. 10b, c). Together, the restored geometries and clumped-isotope temperatures support a vertically extensive fluid-flow system in which faults and fractures linked shallow recharge zones, deeper circulation pathways, and sites of mineral precipitation throughout basin evolution.

Stable isotope compositions provide independent constraints on fluid source. Reconstructed fluid $\delta^{18}O$ values overlap the range of modern meteoric recharge, basin groundwater, and brines reported for Clayton Valley (Gagnon et al., 2023), consistent with dominantly meteoric, basin-buffered fluids. Although reconstructed fluid compositions span a wide range of precipitation temperatures (24.6–139.2 °C; Fig. 8a), these fluid compositions do not require a primary magmatic fluid source. The absence of a systematic shift toward heavier reconstructed fluid $\delta^{18}O$ values with increasing temperature further supports this interpretation. Instead, the elevated precipitation temperatures are interpreted to reflect circulation depth and fluid-rock interaction along structurally focused pathways (e.g., Beaudoin et al., 2022). One sample records a substantially heavier reconstructed fluid composition ($\delta^{18}O$fluid $\approx +3$ ‰ VSMOW), indicating a distinct fluid history involving greater water-rock interaction and/or a less meteoric fluid source.

5.4 Structurally focused fluid circulation and lithium transport in Clayton Valley

Lithium transport and redistribution in Clayton Valley are governed by basin-scale hydrologic processes and lithium availability, with fault and fracture networks likely acting to organize and enhance fluid connectivity and transport efficiency (e.g., Munk et al., 2016; Coffey et al., 2021; Fig. 11). Previous models have emphasized surface weathering of silicic volcanic units, catchment input, and evaporative concentration as primary controls on lithium delivery to the basin

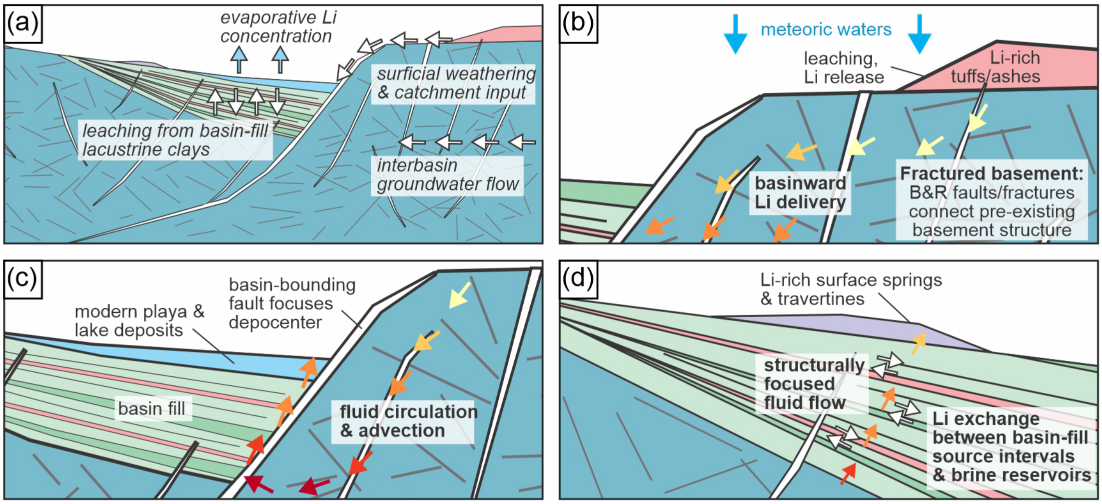

Figure 11. Conceptual model of structurally focused lithium transport and redistribution. **(a)** Previous workers' concepts of lithium transport and delivery at Clayton Valley (e.g., Coffey et al., 2021; Darin et al., 2025). **(b)** Linkage between basement and basin structures, leaching of lithium from silicic volcanic units, fault-controlled delivery of lithium-bearing fluids into developing basin accommodation space. **(c)** Advective circulation involving downwelling cooler fluids and upwelling warmer fluids. **(d)** Lithium exchange between basin-fill source intervals and brine reservoirs. B&R = Basin and Range.

(Fig. 11a). Our results highlight the role of fault and fracture networks in enhancing the efficiency of lithium delivery by focusing fluids derived from surface weathering and shallow groundwater systems into fault-controlled pathways (Fig. 11b–d). Specifically, we provide evidence for (i) long-lived fault and fracture networks that transported lithium over multi-Myr timescales (Figs. 9 and 10), (ii) potential basinward lithium transport and associated advective circulation through fault and fracture networks (Fig. 11b, c), and (iii) structural connectivity also facilitates lithium exchange between basin-fill source intervals, ash- and tuff-hosted aquifers, and evolving brine reservoirs, improving the efficiency of leaching and redistribution processes previously invoked for basin-fill clays (Fig. 11d).

The presence of Basin and Range–age structures that cross-cut and connect pre-existing brittle deformation fabrics and veins (e.g., Figs. 2–4) highlights the propensity for these relatively late structures to link earlier deformation fabrics. These late structures would likely act as permeability backbones that connect fracture networks, enhancing basin-scale connectivity as fault systems grow, interact, and link (cf. Ferrill et al., 2017). In combination, these throughgoing, late-stage structures and connected early features would represent efficient flow pathways for fluids prior to mineralization or when only partially mineralized.

Independent of the ultimate lithium source, the results presented here suggest that faults and fracture networks represent one component of a broader hydrogeologic system that controls lithium mobilization, transport, and enrichment within Clayton Valley. Our results are consistent with recent studies that link lithium enrichment to brittle deformation and faulting in extensional basins (e.g., Marazuela et al., 2020; Benson et al., 2023; Munk et al., 2025; Butler et al., 2025; Putzolu et al., 2025), but extend those interpretations by providing direct evidence that fault-mediated lithium transport and redistribution can occur over million-year timescales. The combined timing, temperature, isotopic, and lithium concentration data demonstrate that fault and fracture networks in Clayton Valley enabled long-lived fluid circulation. Although lithium enrichment ultimately depends on the availability of suitable source materials, groundwater flow, weathering, leaching, and evaporative concentration, our results suggest that long-lived fault and fracture networks may enhance the efficiency of these processes by focusing fluid flow, maintaining hydraulic connectivity through time, and facilitating repeated redistribution of lithium during basin evolution.

6 Conclusions

Fault- and fracture-hosted calcite veins from Clayton Valley record structurally controlled fluid flow spanning at least ∼ 60 to 3.9 Ma. Carbonate U–Pb ages indicate multiple episodes of mineralization, including a principal phase associated with Basin and Range extension between ∼ 15.4 and 3.9 Ma.

Lithium concentrations vary with structural setting, with higher values in basin-fill–hosted veins and paleo-spring travertine deposits and generally lower values in basement-hosted and basin-bounding structures. Consideration of published calcite-fluid lithium partition coefficients suggests that relatively low lithium concentrations in calcite do not necessarily imply lithium-poor parent fluids, highlighting the importance of fluid chemistry and partitioning behaviour when interpreting calcite-hosted lithium records.

Five calcite veins yield U–Pb ages that pre-date emplacement of the ∼ 6 Ma Rhyolite Ridge Tuff, the dominant lithium source reservoir in the region. Although our data do not uniquely identify older lithium source reservoirs, they are compatible with contributions from older lithium-bearing rocks, including Jurassic to Tertiary granitic units exposed around Clayton Valley.

Clumped-isotope temperatures and stable isotope compositions indicate that mineralizing fluids were dominantly meteoric and circulated over a wide range of depths during basin evolution. The combination of meteoric isotopic signatures and elevated precipitation temperatures suggests that warm to hot mineralizing fluids can be generated through structurally controlled circulation and fluid-rock interaction within extensional basin systems, without requiring direct magmatic fluid input.

Faults and fracture networks represent an important component of the broader hydrogeologic system responsible for lithium mobilization and redistribution within Clayton Valley. The combined geochronologic, geochemical, isotopic, and structural data indicate that long-lived fault and fracture networks enhanced fluid connectivity and facilitated repeated fluid circulation and lithium redistribution over million-year timescales.

Data availability. Additional data can be found at https://doi.org/10.5281/zenodo.21343550 (Cawood, 2026).

Supplement. The supplement related to this article is available online at https://doi.org/10.5194/se-17-991-2026-supplement.

Author contributions. AJC contributed to conceptualization, methodology, validation, formal analysis, investigation, data curation, visualization, writing – original draft, supervision, project administration, and funding acquisition. DAF contributed to conceptualization, formal analysis, investigation, writing – original draft, and funding acquisition. IARL contributed to conceptualization, methodology, and investigation. KLB contributed to conceptualization, investigation, and funding acquisition. DEI contributed to conceptualization, methodology, formal analysis, and investigation. ZTS contributed to conceptualization and funding acquisition. MRB contributed to investigation. BS contributed to investigation and/or domain expertise. KJS contributed to investigation and/or domain expertise. LAM contributed to conceptualization. DFB contributed to investigation and/or domain expertise. LDS contributed to methodology, formal analysis, and investigation. DFS contributed to investigation and/or domain expertise. CAG contributed to investigation and/or domain expertise. All authors (AJC, DAF, IARL, KLB, DEI, ZTS, MRB, BS, KJS, LAM, DFB, LDS, DFS, CAG) contributed to writing – review and editing and approved the final manuscript.

Competing interests. The contact author has declared that none of the authors has any competing interests.

Disclaimer. Publisher's note: Copernicus Publications remains neutral with regard to jurisdictional claims made in the text, published maps, institutional affiliations, or any other geographical representation in this paper. The authors bear the ultimate responsibility for providing appropriate place names. Views expressed in the text are those of the authors and do not necessarily reflect the views of the publisher.

Acknowledgements. We thank Albemarle Corporation for data access and field support. We thank the reviewers, Michael Darin and Fabrizio Balsamo, and the editor, Nicolas Beaudoin, for their constructive comments, which improved the manuscript.

Financial support. Financial support was provided by The University of Texas at Dallas Office of Research and Innovation and Southwest Research Institute® SPRINT program (15-R6492), and Southwest Research Institute® Internal Research and Development project 15-R6594.

Review statement. This paper was edited by Nicolas Beaudoin and reviewed by Michael Darin and Fabrizio Balsamo.

References

Albers, J. P. and Stewart, J. H.: Geology and mineral deposits of Esmeralda County, Nevada, Nevada Bureau of Mines and Geology Bulletin, 78, 88 pp., 1972.

ALS: Geochemistry services – lithium, https://www.alsglobal.com/en/geochemistry/energy-minerals-analysis/lithium (last access: 12 February 2025), 2025.

Anderson, N. T., Kelson, J. R., Kele, S., Daëron, M., Bonifacie, M., Horita, J., Mackey, T. J., John, C. M., Kluge, T., Petschnig, P., and Jost, A. B.: A unified clumped isotope thermometer calibration (0.5–1100 °C) using carbonate-based standardization, Geophys. Res. Lett., 48, e2020GL092069, https://doi.org/10.1029/2020GL092069, 2021.

Bailly, P. A.: Geology of the southeastern part of Mineral Ridge, Esmeralda County, Nevada, PhD dissertation, Stanford University, Stanford, California, 1951.

Beaudoin, N. E., Lacombe, O., Hoareau, G., and Callot, J.-P.: How the geochemistry of syn-kinematic calcite cement depicts past fluid flow and assists structural interpretations: a review of concepts and applications in orogenic forelands, Geol. Mag., 159, 2157–2190, https://doi.org/10.1017/S0016756822001327, 2022.

Bense, V. F., Gleeson, T., Loveless, S. E., Bour, O., and Scibek, J.: Fault zone hydrogeology, Earth-Sci. Rev., 127, 171–192, https://doi.org/10.1016/j.earscirev.2013.09.008, 2013.

Benson, T. R., Coble, M. A., and Dilles, J. H.: Hydrothermal enrichment of lithium in intracaldera illite-bearing claystones, Sci. Adv., 9, eadh8183, https://doi.org/10.1126/sciadv.adh8183, 2023.

Bernasconi, S. M., Daëron, M., Bergmann, K. D., Bonifacie, M., Meckler, A. N., Affek, H. P., Anderson, N., Bajnai, D., Barkan, E., Beverly, E., and Blamart, D.: InterCarb: A community effort to improve interlaboratory standardization of the carbonate clumped isotope thermometer using carbonate standards, Geochem. Geophy. Geosy., 22, e2020GC009588, https://doi.org/10.1029/2020GC009588, 2021.

Bhattacharya, T., Brennan, P. R., Ibarra, D. E., Gagnon, C. A., Butler, K. L., Terrazas, A., Miller, S., Munk, L. A., Boutt, D. F., Feng, R., and Bullinger, S. N.: Pleistocene shifts in Great Basin hydroclimate seasonality govern the formation of lithium-rich paleolake deposits, Quaternary Sci. Rev., 335, 108747, https://doi.org/10.1016/j.quascirev.2024.108747, 2024.

Bons, P. D., Elburg, M. A., and Gomez-Rivas, E.: A review of the formation of tectonic veins and their microstructures, J. Struct. Geol., 43, 33–62, https://doi.org/10.1016/j.jsg.2012.07.005, 2012.

Bradley, D. C., Munk, L. A., Jochens, H., Hynek, S., and Labay, K. A.: A preliminary deposit model for lithium brines, U.S. Geological Survey Open-File Report 2013–1006, https://doi.org/10.3133/ofr20131006, 2013.

Bradley, D. C., Stillings, L. L., Jaskula, B. W., Munk, L., and McCauley, A. D.: Lithium, in: Critical Mineral Resources of the United States – Economic and Environmental Geology and Prospects for Future Supply, edited by: Shultz, K. J., DeYoung, J. H., Seal, R. R., and Bradley, D. C., U.S. Geological Survey Professional Paper 1802, K1–K21, https://doi.org/10.3133/pp1802K, 2017.

Brand, W. A., Assonov, S. S., and Coplen, T. B.: Correction for the 17O interference in δ13C measurements when analyzing CO2 with stable isotope mass spectrometry (IUPAC Technical Report), Pure Appl. Chem., 82, 1719–1733, https://doi.org/10.1351/PAC-REP-09-01-05, 2010.

Branson, O., Uchikawa, J., Bohlin, M. S., and Misra, S.: Controls on Li partitioning and isotopic fractionation in inorganic calcite, Geochim. Cosmochim. Acta, 382, 91–102, https://doi.org/10.1016/j.gca.2024.07.001, 2024.

Butler, K. L., Munk, L. A., Boutt, D. F., Morris, N., Kennedy, J., Saha, P., Blake, M. R., Custado, M. J., and Ibarra, D. E.: The origin and enrichment of sedimentary basin lithium brines: A case study from the Upper Devonian Leduc Formation, Alberta Basin, Canada, Econ. Geol., 120, 649–662, https://doi.org/10.5382/econgeo.5151, 2025.

Caine, J. S., Evans, J. P., and Forster, C. B.: Fault zone architecture and permeability structure, Geology, 24, 1025–1028, https://doi.org/10.1130/0091-7613(1996)024<1025:FZAAPS>2.3.CO;2, 1996.

Cawood, A. J.: Supplemental data for "Structural controls on lithium-bearing fluid flow in Clayton Valley, Nevada", Zenodo [data set], https://doi.org/10.5281/zenodo.21343550, 2026.

Cawood, A. J., Ferrill, D. A., Morris, A. P., Norris, D., McCallum, D., Gillis, E., and Smart, K. J.: Tectonostratigraphic evolution of the Orphan Basin and Flemish Pass region – Part 1: Results from coupled kinematic restoration and crustal area balancing, Mar. Petrol. Geol., 128, 105042, https://doi.org/10.1016/j.marpetgeo.2021.105042, 2021.

Cawood, A., Ferrill, D., Rangel-Landeros, I., Butler, K., Sickmann, Z., Blake, M., Ibarra, D., Swanson, B., Munk, L., Boutt, D., Stockli, L., Stockli, D., and Gagnon, C.: Geochemical constraints on lithium transport in fault and fracture systems, Geological Society of America Abstracts with Programs, 57, 272-9, https://doi.org/10.1130/abs/2025AM-8723, 2025.

Chen, T. W., Smye, A., Lloyd, M., Fisher, D., and Hashimoto, Y.: Temperatures of vein formation associated with plate interface deformation constrained by oxygen and clumped isotope thermometry, Geochem. Geophy. Geosy., 25, e2024GC011516, https://doi.org/10.1029/2024GC011516, 2024.

Chew, D. M., Petrus, J. A., and Kamber, B. S.: U–Pb LA–ICP–MS dating using accessory mineral standards with variable common Pb, Chem. Geol., 363, 185–199, https://doi.org/10.1016/j.chemgeo.2013.11.006, 2014.

Coffey, D. M., Munk, L. A., Ibarra, D. E., Butler, K. L., Boutt, D. F., and Jenckes, J.: Lithium storage and release from lacustrine sediments: Implications for lithium enrichment and sustainability in continental brines, Geochem. Geophy. Geosy., 22, e2021GC009916, https://doi.org/10.1029/2021GC009916, 2021.

Daëron, M., Blamart, D., Peral, M., and Affek, H. P.: Absolute isotopic abundance ratios and the accuracy of Δ47 measurements, Chem. Geol., 442, 83–96, https://doi.org/10.1016/j.chemgeo.2016.08.014, 2016.

Darin, M. H., Harlaux, M., Ogilvie, I. A., Reynolds, J. T., and Chafetz, D. A.: Source-to-sink evolution of volcano-sedimentary Li–B deposits at Rhyolite Ridge, southwestern Nevada, Econ. Geol., 120, 1167–1190, https://doi.org/10.5382/econgeo.5152, 2025.

Davis, G. H., Bos Orent, E., Clinkscales, C., Ferroni, F. R., Gehrels, G. E., George, S. W. M., Guns, K. A., Hanagan, C. E., Hughes, A. N., Iriondo, A., Jepson, G., Kelty, C., Krantz, R. W., Levenstein, B. M., Lingrey, S. H., Miggins, D. P., Moore, T., Portnoy, S. E., Reeher, L. J., and Wang, J. W.: Structural analysis and chronologic constraints on progressive deformation within the Rincon Mountains, Arizona: Implications for development of metamorphic core complexes, Geol. Soc. Am. Mem., 222, 1–125, https://doi.org/10.1130/2023.1222(01), 2023.

Davis, J. R. and Vine, J. D.: Stratigraphic and tectonic setting of the lithium brine field, Clayton Valley, Nevada, Rocky Mountain Association of Geologists Basin and Range Symposium, 421–430, 1979.

Davis, J. R., Friedman, I., and Gleason, J. D.: Origin of the lithium-rich brine, Clayton Valley, Nevada, U.S. Geological Survey Bulletin, 1622, 131–138, 1986.

Diamond, D. and Ingersoll, R.: Structural and sedimentologic evolution of a Miocene supradetachment basin, Silver Peak Range and adjacent areas, west-central Nevada, Int. Geol. Rev., 44, 588–623, https://doi.org/10.2747/0020-6814.44.7.588, 2002.

Drake, H., Mathurin, F. A., Zack, T., Schäfer, T., Roberts, N. M., Whitehouse, M., Karlsson, A., Broman, C., and Åström, M. E.: Incorporation of metals into calcite in a deep anoxic granite aquifer, Environ. Sci. Technol., 52, 493–502, https://doi.org/10.1021/acs.est.7b05258, 2018.

Eaton, G. P.: The Basin and Range province: Origin and tectonic significance, Annu. Rev. Earth Pl. Sc., 10, 409–440, https://doi.org/10.1146/annurev.ea.10.050182.002205, 1982.

Ferrill, D. A., Morris, A. P., McGinnis, R. N., and Smart, K. J.: Myths about normal faulting, Geological Society, London, Special Publications, 439, 41–56, https://doi.org/10.1144/SP439.12, 2017.

Ferrill, D. A., Smart, K. J., Cawood, A. J., and Morris, A. P.: The fold-thrust belt stress cycle: Superposition of normal, strike-slip, and thrust faulting deformation regimes, J. Struct. Geol., 148, 104362, https://doi.org/10.1016/j.jsg.2021.104362, 2021.

Folk, R. L.: Practical petrographic classification of limestones, AAPG Bull., 43, 1–38, https://doi.org/10.1306/0BDA5C36-16BD-11D7-8645000102C1865D, 1959.

Folk, R. L.: Spectral subdivision of limestone types, in: Classification of Carbonate Rocks, edited by: Ham, W. E., AAPG Memoir., 1, 62–84, 1962.

Folk, R. L.: Some aspects of recrystallization in ancient limestones, in: Dolomitization and Limestone Diagenesis, edited by: Pray, L. C. and Murray, R. C., SEPM Spec. P., 13, 14–48, https://doi.org/10.2110/pec.65.07.0014, 1965.

Füger, A., Konrad, F., Leis, A., Dietzel, M., and Mavromatis, V.: Effect of growth rate and pH on lithium incorporation in calcite, Geochim. Cosmochim. Acta, 248, 14–24, https://doi.org/10.1016/j.gca.2018.12.040, 2019.

Fyfe, W. S., Price, N. J., and Thompson, A. B.: Fluids in the Earth's crust, Elsevier, Amsterdam, ISBN 9780444416360, 1978.

Gagnon, C. A., Butler, K. L., Gaviria, E., Terrazas, A., Gao, A., Bhattacharya, T., Boutt, D. F., Munk, L. A., and Ibarra, D. E.: Paleoclimate controls on lithium enrichment in Great Basin Pliocene–Pleistocene lacustrine clays, Geol. Soc. Am. Bull., 135, 3201–3212, 2023.

Ghosh, P., Adkins, J., Affek, H., Balta, B., Guo, W., Schauble, E. A., Schrag, D., and Eiler, J. M.: 13C–18O bonds in carbonate minerals: A new kind of paleothermometer, Geochim. Cosmochim. Ac., 70, 1439–1456, https://doi.org/10.1016/j.gca.2005.11.014, 2006.

Guillong, M., Samankassou, E., Müller, I. A., Szymanowski, D., Looser, N., Tavazzani, L., Merino-Tomé, Ó., Bahamonde, J. R., Buret, Y., and Ovtcharova, M.: Technical note: RA138 calcite U–Pb LA-ICP-MS primary reference material, Geochronology, 6, 465–474, https://doi.org/10.5194/gchron-6-465-2024, 2024.

Hancock, P. L.: Brittle microtectonics: Principles and practice, J. Struct. Geol., 7, 437–457, https://doi.org/10.1016/0191-8141(85)90048-3, 1985.

Heilweil, V. M. and Brooks, L. E. (Eds.): Conceptual model of the Great Basin carbonate and alluvial aquifer system, U.S. Geological Survey Scientific Investigations Report 2010–5193, 191 pp., https://doi.org/10.3133/sir20105193, 2011.

Hollocher, K. and Ruiz, J.: Major and trace element determinations on NIST glass standard reference materials by inductively coupled plasma mass spectrometry, Geostandard. Newslett., 19, 27–34, https://doi.org/10.1111/j.1751-908X.1995.tb00149.x, 1995.

Jochum, K. P., Willbold, M., Raczek, I., Stoll, B., and Herwig, K.: Chemical characterisation of USGS reference glasses using multiple techniques, Geostand. Geoanal. Res., 29, 285–302, https://doi.org/10.1111/j.1751-908X.2005.tb00901.x, 2005.

Kaiyun, C., Honglin, Y., Zhian, B., Chunlei, Z., and Mengning, D.: Precise in situ determination of lead isotope ratios using femtosecond laser ablation MC-ICP-MS, Geostand. Geoanal. Res., 38, 5–21, 2014.

Kim, S. T. and O'Neil, J. R.: Equilibrium and nonequilibrium oxygen isotope effects in synthetic carbonates, Geochim. Cosmochim. Ac., 61, 3461–3475, https://doi.org/10.1016/S0016-7037(97)00169-5, 1997.

Kunasz, I. A.: Lithium occurrence in the brines of Clayton Valley, Esmeralda County, Nevada, Proceedings of the Fourth Symposium on Salt, 57–66, 1974.

Marazuela, M. A., Ayora, C., Vázquez-Suñé, E., Olivella, S., and García-Gil, A.: Hydrogeological constraints for lithium enrichment in the Salar de Atacama, Sci. Total Environ., 739, 139959, https://doi.org/10.1016/j.scitotenv.2020.139959, 2020.

Munk, L., Jochens, H., Jennings, M., Bradley, D., Hynek, S., and Godfrey, L.: Geochemistry of lithium-rich brines in Clayton Valley, Nevada, Proceedings of the 11th SGA Biennial Meeting, 217–219, 2011.

Munk, L. A., Hynek, S. A., Bradley, D., Boutt, D. F., Labay, K., and Jochens, H.: Lithium brines: A global perspective, Rev. Econ. Geol., 18, 339–365, https://doi.org/10.5382/Rev.18.14, 2016.

Munk, L. A., Boutt, D., Butler, K., Russo, A., Jenckes, J., Moran, B., and Kirshen, A.: Lithium brines: Origin, characteristics, and global distribution, Econ. Geol., 120, 575–597, https://doi.org/10.5382/econgeo.5134, 2025.

Ogilvie, I., Darin, M. H., Reynolds, J. T., Chafetz, D. A., and Harlaux, M.: Geologic map of Rhyolite Ridge and the northern Silver Peak Range, Esmeralda County, Nevada, Nevada Bureau of Mines and Geology Open-File Report 2023-11, scale 1 : 24 000, 35 pp., 2023.

Ogilvie, I. A.: Structure, stratigraphy, and source of sediment-hosted lithium deposits at Rhyolite Ridge, Silver Peak Range, western Nevada, MSc thesis, University of Nevada-Reno, Reno, Nevada, 153 pp., 2023.

Oldow, J. S., Kohler, G., and Donelick, R. A.: Late Cenozoic extensional transfer in the Walker Lane strike-slip belt, Nevada, Geology, 22, 637–640, https://doi.org/10.1130/0091-7613(1994)022<0637:LCETIT>2.3.CO;2, 1994.

Oldow, J. S., Geissman, J. W., and Stockli, D. F.: Evolution of late Neogene transtension in structural stepovers linking the Walker Lane and Eastern California Shear Zone, Int. Geol. Rev., 50, 1–21, 2008.

Olson, J. C. and Hinrichs, E. N.: Beryl-bearing pegmatites in the Ruby Mountains and other areas in Nevada and northwestern Arizona, U.S. Geological Survey Bulletin, 1082-D, D135–D200, https://doi.org/10.3133/b1082D, 1960.

Palacios-García, N. B., Fitz-Díaz, E., Stockli, L. D., and Stockli, D. F.: U–Pb calcite dating of brittle deformation in Permian carbonates, J. Struct. Geol., 171, 104863, https://doi.org/10.1016/j.jsg.2023.104863, 2023.

Papke, K. G.: Evaporites and brines in Nevada playas, Nevada Bureau of Mines and Geology Bulletin, 87, 35 pp., 1976.

Paton, C., Hellstrom, J., Paul, B., Woodhead, J., and Hergt, J.: Iolite: Freeware for the visualisation and processing of mass spectrometric data, J. Anal. Atom. Spectrom., 26, 2508–2518, https://doi.org/10.1039/C1JA10172B, 2011.

Price, J. G., Lechler, P. J., Lear, M. B., and Giles, T. F.: Possible volcanic sources of lithium in Clayton Valley, Nevada, Geological Society of Nevada Symposium Proceedings, 241–248, 2000.

Putzolu, F., Armstrong, R. N., Benson, T. R., Boutt, D. F., Butler, K. L., Dolgopolova, A., Herrington, R. J., Ibarra, D. E., and Munk, L. A.: Volcano-sedimentary deposits: Overview of an emerging type of lithium resource, Econ. Geol., 120, 541–573, https://doi.org/10.5382/econgeo.5135, 2025.

Rangel, I., Cawood, A., Butler, K., Sickmann, Z., Blake, M., Swanson, B., Ibarra, D., Gagnon, C., Munk, L., Boutt, D., Ferrill, D., and Smart, K.: Revised tectonic framework for the Clayton Valley lithium deposits, Geological Society of America Abstracts with Programs, 57, 272-3, 2025.

Roberts, N. M. W. and Holdsworth, R. E.: Timescales of faulting through calcite geochronology: A review, J. Struct. Geol., 158, 104578, https://doi.org/10.1016/j.jsg.2022.104578, 2022.

Roberts, N. M. W. and Walker, R. J.: U–Pb geochronology of calcite-mineralized faults: Absolute timing of rift-related fault events on the northeast Atlantic margin, Geology, 44, 531–534, https://doi.org/10.1130/G37868.1, 2016.

Roberts, N. M., Rasbury, E. T., Parrish, R. R., Smith, C. J., Horstwood, M. S., and Condon, D. J.: A calcite reference material for LA-ICP-MS U–Pb geochronology, Geochem. Geophy. Geosy., 18, 2807–2814, https://doi.org/10.1002/2016GC006784, 2017.

Stewart, J. H.: Regional characteristics, tilt domains, and extensional history of the Basin and Range province, Geol. Soc. Am. Spec. Pap., 323, 47–74, 1998.

Stewart, J. H. and Diamond, D. S.: Changing patterns of extensional tectonics, Geol. Soc. Am. Mem., 176, 447–475, 1990.

Teng, F. Z., McDonough, W. F., Rudnick, R. L., Dalpé, C., Tomascak, P. B., Chappell, B. W., and Gao, S.: Lithium isotopic composition and concentration of the upper continental crust, Geochim. Cosmochim. Ac., 68, 4167–4178, https://doi.org/10.1016/j.gca.2004.03.031, 2004.

Tera, F. and Wasserburg, G. J.: U–Th–Pb systematics in lunar highland samples, Earth Planet. Sc. Lett., 17, 36–51, https://doi.org/10.1016/0012-821X(72)90257-9, 1972.

Thompson, A. L., Richardson, C. A., Gootee, B. F., Wilkins, J., and Fenerty, B.: Geology, geochemistry, and potential origins of the Basin volcano-sedimentary lithium deposit, Econ. Geol., 120, 663–688, https://doi.org/10.5382/econgeo.5138, 2025.

U.S. Geological Survey: Quaternary fault and fold database for the United States, https://www.usgs.gov/publications/quaternary-fault-and-fold-database-united-states (last access: 31 December 2024), 2024.

Vermeesch, P.: IsoplotR: A free and open toolbox for geochronology, Geosci. Front., 9, 1479–1493, https://doi.org/10.1016/j.gsf.2018.04.001, 2018.

Watts, K. E.: Lithium from magma to mine in an early Yellowstone hotspot caldera, Geology, 53, 592–596, https://doi.org/10.1130/G53140.1, 2025.